Chapter2

Benzylic C_{sp3}-H Bond Oxidation on (111) Facets of *o*-Cu_2O Nanocrystals: C-H Bond Activation through Semiconductor Facets Mediated Catalysis.

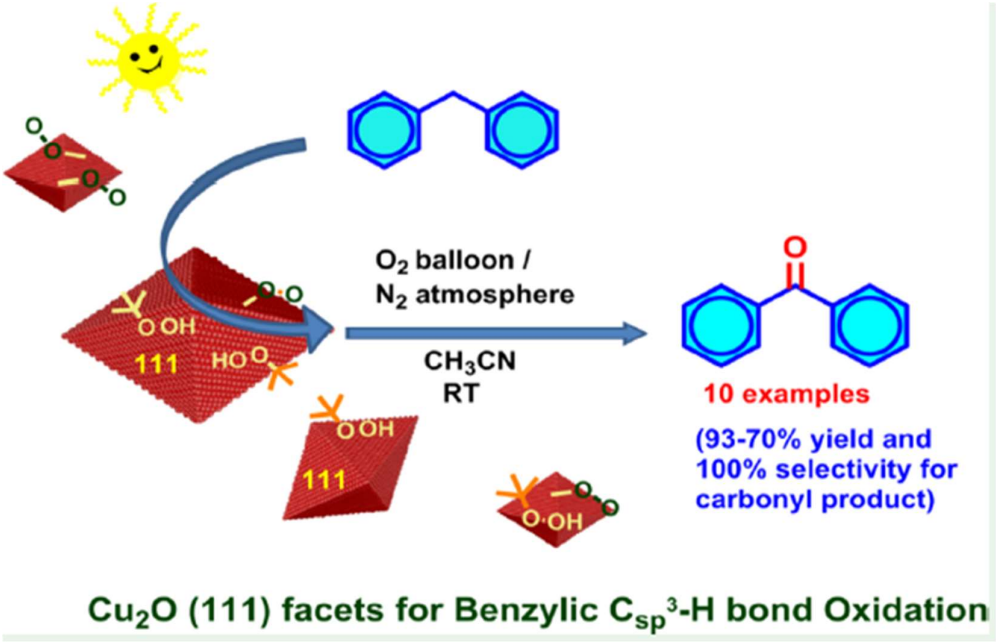

Cu_2O (111) facets for Benzylic C_{sp}^3-H bond Oxidation

2.1 Introduction

Selective functionalization of C−H bonds is challenging since it requires the activation of a stubborn C−H bond/s toward the reagents or catalytic systems. This protocol is important in organic synthesis as it can reduce many steps toward the target product in total synthesis and save precious resources and affect the overall cost. Direct benzylic oxidation has been applied extensively for the synthesis of pharmaceuticals and fine chemicals, and this approach has enjoyed significant commercial success. A wide range of commercially available pharmaceutical drugs has one or more oxidized benzylic positions involved in their structure (Fig. 2.1).[1] Many strategies have been developed for this purpose. The methods involving activation of benzylic sp^3 C−H bonds and their direct oxidation to aromatic carbonyl have particular importance due to their applications in pharmaceutical industries as API.

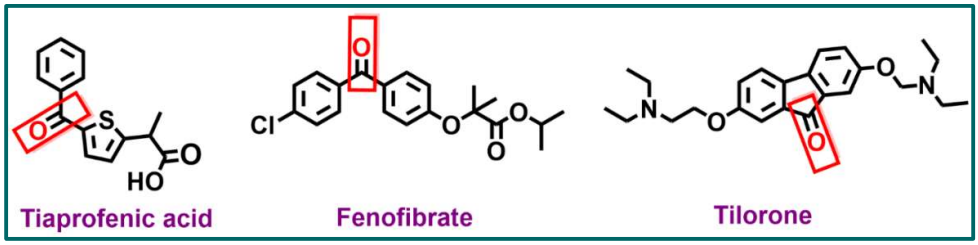

Fig. 2.1 Benzylic C−H Oxygenated Pharmaceutical Compounds.

Development of the mild reagents or the catalytic systems that can functionalize the desired C-H bonds in the complex molecular framework at any stage of synthesis (late-stage functionalization) without affecting the surrounding molecular environment is the "holy grail" of chemistry[2] Direct oxidation of benzylic sp^3 C-H to carbonyl is tricky and involves metals like Au, (Scheme 2.1) [3] Pd, [4]Rh, ($Rh_2(esp)_2$) (Fig 2.2) [5], and Re (Scheme 2.2) (group 4d and 5d metals)-mediating catalysis.

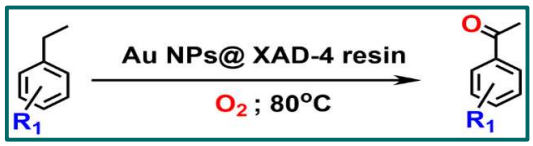

Scheme 2.1 Oxidation of alkyl-substituted benzene by AuNPs@ resin.

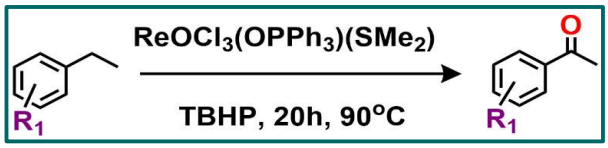

Scheme 2.2 Oxidation of alkyl-substituted benzene by Re salts.

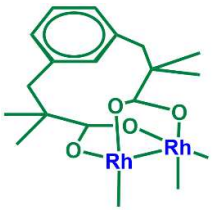

Fig. 2.2 $Rh_2(esp)_2$ structure.

The Friedel-Crafts acylation of aromatics is a well-known synthesis protocol for this purpose. However, it involves metal halide-based Lewis acid catalysis. Strong oxidizing agents like acidic solutions of $KMnO_4$ or CrO_3 can do the same job. However, these protocols produce environmentally toxic by-products during the processing. Oxidation processes involving molecular oxygen or reactive oxygen species (ROSs) as oxidants in an aqueous medium at RT in the presence of a mild catalytic system should be the best.

Metal-free catalytic systems, for this purpose, were developed in the past. For example, Zhang et al. developed an I_2-pyridine-TBHP (t-butyl hydroperoxide) system for the solvent-free oxidation of benzylic methylene to ketone at 80 °C, heated in a sealed tube.[6] Here, I_2-Py acting as a co-catalyst forms the "outer complex" and, in turn, generates PYİ free radical responsible for activating the benzylic C-H bond for oxidation.

Stahl et al. recently reported the cobalt(II)/N-hydroxypthalimide (NHPI) catalyst system for the selective conversion of benzylic methylene group in pharmaceutically relevant (hetero) arenes to the corresponding (hetero) aryl ketones (Scheme 2.3).[7]

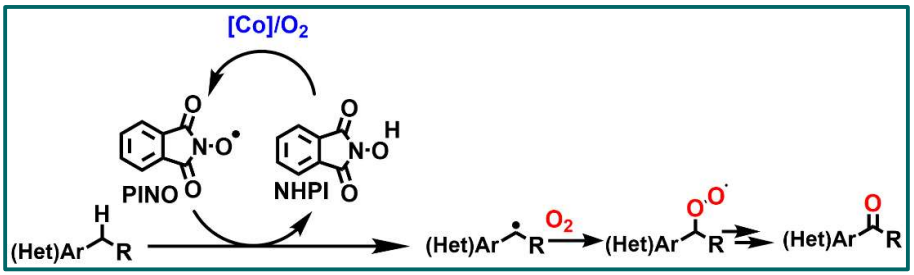

Scheme 2.3 Cobalt(II)/N-hydroxypthalimide (NHPI) catalyst system for oxidation.

These reactions were mediated by free radical pathway under reaction conditions like a solution of 1 M substrate in BuOAc or EtOAc as a solvent, 12 h time, and 90-100 °C temperature. However, they observed that some substrates make chelate with cobalt to attenuate its catalytic activity. To overcome this, they developed an NHPI catalysed electrochemical oxygenation method. Wang and Li also developed TEMPO-derived sulfonic salt as a catalyst for aerobic oxidation of benzylic sp^3 C-H bonds of ethers and alkyl arenes with $NaNO_2$ and HCl co catalysts in the presence of O_2 as an oxidant (Scheme 2.4).

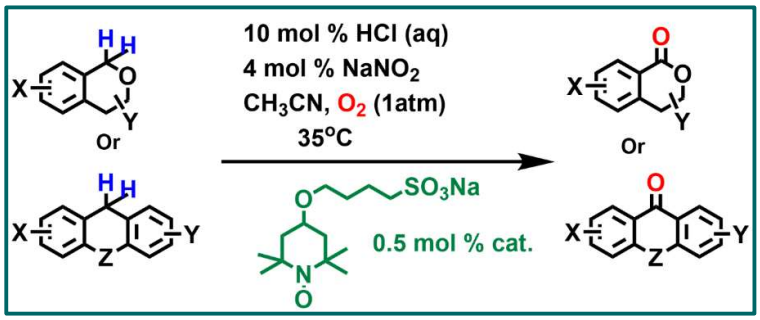

Scheme 2.4 TEMPO-derived sulfonic salt as a catalyst for oxidation.

Wang et al. developed this kind of reaction for the room temperature oxidation of heterobenzylic sp^3 C –H bond.[31] They carried out this reaction in DMF in the presence of KO^{t}Bu as a promoter and molecular oxygen as the oxidant. However, this protocol requires additive like TMEDA, PEG-300, or 18-crown-6 under basic conditions due to KO^{t}Bu (Scheme 2.5).

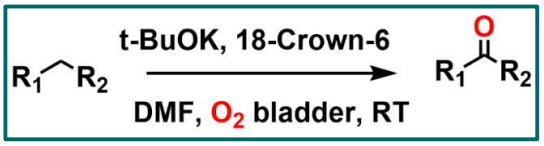

Scheme 2.5 Crown ether for oxidation.

Lei et al. reported 9-mesityl-10-methyl acridinium chlorate (Acr^{+-}mes ClO_4^-) as a photo-catalyst for benzylic sp^3 C-H bond oxidation by molecular oxygen in the presence of visible light (Scheme 2.6).[8]

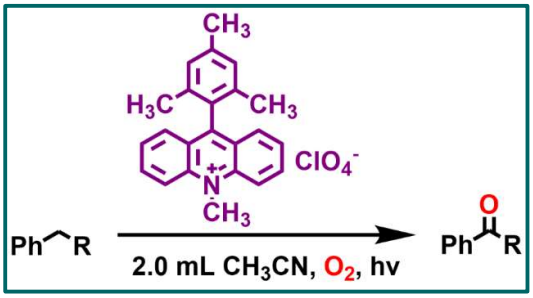

Scheme 2.6 Photocatalyst (9-mesityl-10-methyl acridinium chlorate (Acr^{+-}mes ClO_4^-)) for oxidation.

Recently, Li et al. reported Cu(II)/{PMo_{12}} catalytic system for the benzylic C-H oxidation.[21] This system works in the solution of TBHP in a 1:1 mixture of H_2O and CH_3CN at 90°C (Scheme 2.7).

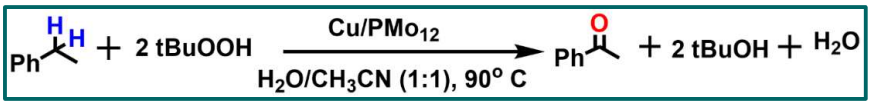

Scheme 2.7 POM as a catalyst for oxidation

2.2 Synthesis of *o*-Cu_2O NCs.

Chemicals: Copper acetate monohydrate ($Cu(CH_3COO)_2.H_2O$ AR), adamantine, and camphor were purchased from Sigma-Aldrich chemicals, Germany. Ascorbic acid ($C_6H_8O_6$, AR), sodium hydroxide, and ethylbenzene were purchased from S.D. fine Chemical Ltd., Mumbai, India. Polyvinyl alcohol ($(C_2H_4O)_x$) diphenylmethane, cyclohexanone, cyclohexane, and tetrahydrofuran were purchased from Loba Chemie Pvt. Ltd., Mumbai, India, Benzhydrol, 4-ethylnitrobenzene, fluorene, indane, tetralin and 4-benzylphenol, 4-ethylanisol, 9,10-dihydroanthracene, 4-ethylaniline all were purchased from TCI Chemicals (India) Pvt. Ltd, isobutylbenzene from Spectrochem Pvt. Ltd. All the chemicals were used without further purification. Freshly prepared deionised water was used for the synthesis of the *o*-Cu_2O NCs.

6.0 mmol of cupric acetate ($Cu(CH_3COO)_2$. H_2O) and 0.12 mmol (in repeating unit) of polyvinyl alcohol (PVA) were dissolve in 50.0 mL water at 60 ºC. First, the light blue color solution was stirred for 1h. Then, the aqueous solution of NaOH (120 mmol, 4.8g in 20.0 mL) was added dropwise under vigorous stirring. The appearance of dark blue color indicates the formation of cupric hydroxide ($Cu(OH)_2$). Then 20.0 mL aqueous solution of ascorbic acid (18.0 mmol) was added quickly in the above suspension under vigorous stirring, and the color of suspension changes from blue to green and finally to reddish after 30 min of stirring (Fig.2.3) The reaction mixture was centrifuged at 6000 rpm for 10 min. The collected product was washed with DI water (5 times) and finally with absolute alcohol and dried in hot air oven at 60 ºC.

Fig. 2.3 The appearance of the reaction mixture at the end of 30 min of stirring of required reactants under the conditions mentioned in the experimental section, indicating the formation of *o*-Cu_2O NCs. The NCs were synthesized by using method reported in the literature with modifications.[9]

2.3 Characterization.

Powder X-ray diffraction (XRD) pattern was obtained using a PANalytical X-ray diffractometer operated with Cu Kα radiation, λ = 0.15418 nm. The morphology with elemental analysis of the samples was examined by FESEM (JEOL-JSM-7100F). The particle size determination with elemental mapping was carried out by TEM (JEOL-JEM-2100) at 200 kV. The oxidation state and surface chemical composition of nanoparticles were measured using X-ray photoelectron spectroscopy, in a Scient Omicron Multiprobe (MXPS) spectrometer, equipped with an XM 1000 X-ray monochromator. A typical Al Kα (1486.6 eV) source was used for X-ray radiation. The sample from the ongoing reaction mixture was collected at the end of the 2nd day and mixed with the solution of TEMPO as a spin trapping agent immediately before the EPR measurement. The prepared sample was transferred to a small quartz flat cell of the spectrometer (X-band EPR spectrometer, BioSpin, Bruker). Initially, we put the sample inside the EPR tube. The EPR tube was kept inside the central cavity part of the Instrument. After fixing this EPR tube inside the cavity of the instrument, the sample was tuned using the command 'Auto Tune' and the value of center EPR spectrum was recorded. The samples were degassed at 80 °C prior to Brunauer-Emmett-Teller (BET) measurements. The BET surface area was determined by nitrogen adsorption (Micrometrics ASAP 2020) via a multipoint BET method using the adsorption data in the relative pressure (P/P0) range of 0.0-1.0. The desorption isotherm was used to determine the pore size distribution using the Barrett−Joyner-Halenda (BJH) method, assuming a cylindrical pore model. The nitrogen adsorption volume at the relative pressure (P/P_0) of 0.997 was used to determine the pore volume and average pore size. The FTIR (PerkinElmer, Spectrum Two) spectra of the synthesized products were obtained in the range of 400-4000 cm^{-1}. 1H NMR and 13C NMR spectra of the products were recorded on a Bruker Avance 300 MHz spectrometer using TMS as an internal standard in $CDCl_3$. All of the spectra are reported in the last section of chapter. Cyclic voltammetry (CV) was performed using a threeelectrode system comprising platinum disk, platinum wire, and saturated calomel electrode as working, counter, and reference electrodes, respectively. The Cu_2O powder-coated platinum electrode was taken as the working electrode. CV was carried out in the potential range of -1.3 to 1.5 V with a scan rate of 50 mV s^{-1} in the dark and 0.2 sun light illumination. The Mott−Schottky (MS) measurement was carried out in the potential range of 1.0-2.5 V using the aforementioned electrode system with aqueous 0.1 M KCl solution. The CV and MS measurements were performed using electrochemical workstation, CHI660E (CHI Instruments, Austin TX). To investigate the conductivity, the electrochemical impedance field

was fixed at 3100G, sweep width -4000, Mod frequency-100Hz, Mod Amplitude -10 G, conversion -50 ms, time constant 20 ms. After fixing all of these values, the EPR signals were collected and the spectroscopy (EIS) was tooled by sweeping a frequency ranging from 1.2 MHz to 0.1 Hz with an amplitude AC signal of 10 mV using a Solartron 1260 + 1287 interface. The EIS measurements were carried out by sandwiching the Cu_2O pellet between two fluorine-doped tin oxide (FTO)-coated glass plates (15 Ω, Solaronix, Switzerland). The EIS measurements were performed in the dark and light illumination of 1 sun (100 mW cm^{-2}) provided through a 100 W xenon lamp of solar simulator (PET, Inc.). From the EIS, conductivity was calculated by [10] $\sigma = l/RbA$ where σ is the conductivity in S cm^{-1}, Rb is the ohmic resistance of the Cu_2O sample, l is the distance between the two SS electrodes, and A is the total area of the pellet. The hydrodynamic size of nanoparticles was calculated using a BIC 90 plus (Brookhaven) equipped with 35.0 mW solid-state lasers operating at 660 nm, and surface charge (ξ- potential) measurement was carried out using an avalanche photodiode detector. DFT simulation: Plane-wave DFT calculations were performed using the Quantum Espresso package[11]. The calculations were carried out with the PBE-D3 (BJ) + U (Perdew-Burke-Ernzerhof functional combined with Grimme's D3 (BJ) + Hubbard term (U) correction and henceforth denoted by the PBED3(BJ) + U) level theory [12] using a U-J value of 6 eV for the Cu dstate corrections. All of the valence electrons (Cu: $3d^{10}4s^1$, O: $2s^22p^4$) were treated explicitly, employing a plane-wave cutoff of 60 Ry. A 5 × 5 × 1 Monkhorst-Pack60 k-point sampling grid was used for the Brillouin zone integration along with Marzari-Vanderbilt cold smearing [13] of 0.01 Ry throughout the calculations. The geometry optimization was carried out until the residual force on each atom was smaller than 10^{-4} eV Å-1. The 3 × 3 supercell for the Cu_2O (111) surface was modelled as periodic slab consisting of three Cu_2O layers, with a vacuum distance of 15 Å between the two successive images of the slab. The top two Cu_2O layers were allowed to relax in all calculations.

2.4 Result and Discussion

The phase and purity of synthesized *o*-Cu_2O NCs were studied by powder X-ray diffraction (PXRD) analysis. The XRD pattern manifests predominant diffraction peaks at 2θ values of 29.65, 36.52, 42.42, 61.55, 73.73, and 77.61°corresponding to the refraction from (110), (111), (200), (220), (311), and (222) planes (Fig. 2.4), confirming the cuprite phase of Cu_2O (JCPDS# 77-0199). Energy-dispersive X-ray analysis (EDAX) also reveals the phase purity of the material. It can be observed from the XRD pattern that the (111) refraction peak is higher in intensity with a high (111)/(200) intensity ratio suggesting the exclusive exposure of (111)

planes of NCs.[14] Hence, it is confirmed from the XRD study that the synthesized Cu_2O NCs are highly phase-pure, having octahedron morphology. The crystallite size, calculated by the Debye-Scherrer formula ($L = 0.9\lambda/\beta \cos\theta$) and the full width at half-maximum (FWHM) value of the significant peak for (111) planes, is in the range of 42 nm.[15] The size and morphology of Cu_2O nanoparticles were also confirmed using field emission scanning electron microscopy (FESEM) and high-resolution transmission electron microscopy (HRTEM) analyses (Fig. 2.5 and Fig. 2.6).

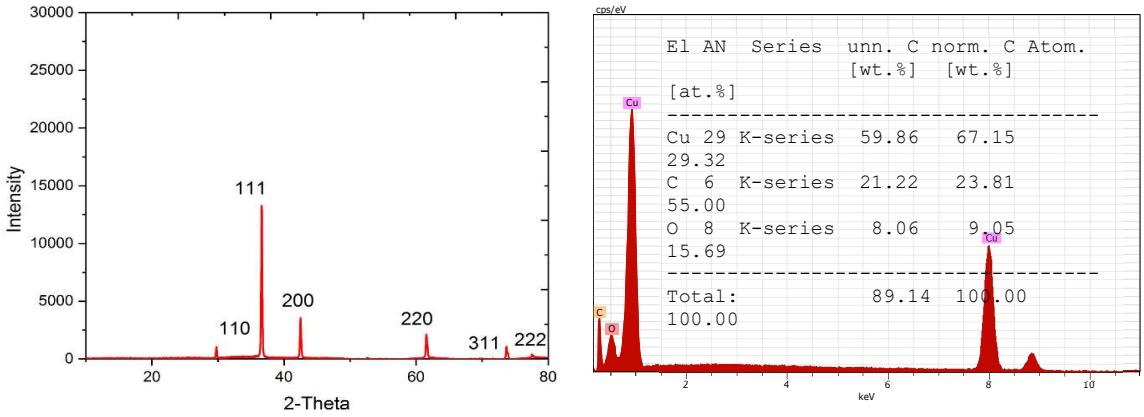

Fig. 2.4 (A) XRD patterns (JCPDS 77-0199) and (B) EDAX elemental analysis.

FESEM images and the size histogram show a uniform size distribution of *o*-Cu_2O NCs (Fig. 2.5.) It can be observed that all of the eight (111) facets of octahedral crystals are depressed at the center. The average particle size of the synthesized octahedra is found to be 143.3 nm. The crystallographic features of this octahedral morphology were also studied using TEM and the corresponding selected area electron diffraction (SAED) analysis. Fig. 2.6 shows the HRTEM image. The vertical alignment of an electron beams to (111) facets formed a two-dimensional (2-D) hexagonal projection. In a cluster of three hexagons, the central one is attached with the other two through (111) facets. A slight truncation with the emergence of (100) planes can also be observed. An apparent 125° angle among the sharp (111) edges can provide a site for the catalytic reaction. It can also be seen that the edges of each side are thinner than the central part, which creates a bright contrast due to minor depression at each edge, also confirmed by the HRTEM images. The lattice fringes in (Fig. 2.6 C) can be indexed to the (111) planes of the octahedral facet (d (111) = 0.24 nm). The fast Fourier transform pattern generated from the crystal lattices produces the diffraction spots in the direction vertical to the alignment of fringes, further confirming the crystallinity of the material. From this study, the mode of Cu_2O crystal growth and the role of the capping agent (CA) can be envisaged. It was demonstrated

that the cube-shaped particles are a thermodynamically stable form of cuprite Cu_2O in the absence of CA. There is a systematic change in this basic shape from cubic through truncated cubes to cuboctahedron by varying CA-to-copper precursor ratio.[16] In the present study, we have used poly (vinyl alcohol) (PVA) as a CA adsorbed on the polar oxygen-ended (100) facets of the cube morphology due to H-bonding that hinders the growth of (100) facets, resulting in octahedron morphology having triangular (111) facets. We have stringently maintained all of the reaction parameters during the experimental procedure to achieve octahedral morphology; however, we cannot omit crystals of other shapes (like dodecahedra and cube) in minute quantity. Once the targeted morphology (octahedral) was achieved (the reddish-brown color after 90 min), the crystals were washed thoroughly with deionized water and then with ethanol thrice to ensure the complete removal of the capping agent; this, in turn, nullifies the interference of CA during organic transformation. The removal of CA was confirmed from Fourier transform infrared (FTIR) spectra (Fig. 2.7). If PVA is bound firmly on the surface, the broad V-shaped hump around 3500-3600 cm^{-1} would appear, which is absent in our case. The small humps around 3500 and 3000 cm^{-1} are due to surface-adsorbed water and CO_2 during washing and experimental end procedures. The band at 632 cm^{-1} is due to Cu(I)-O vibrations.

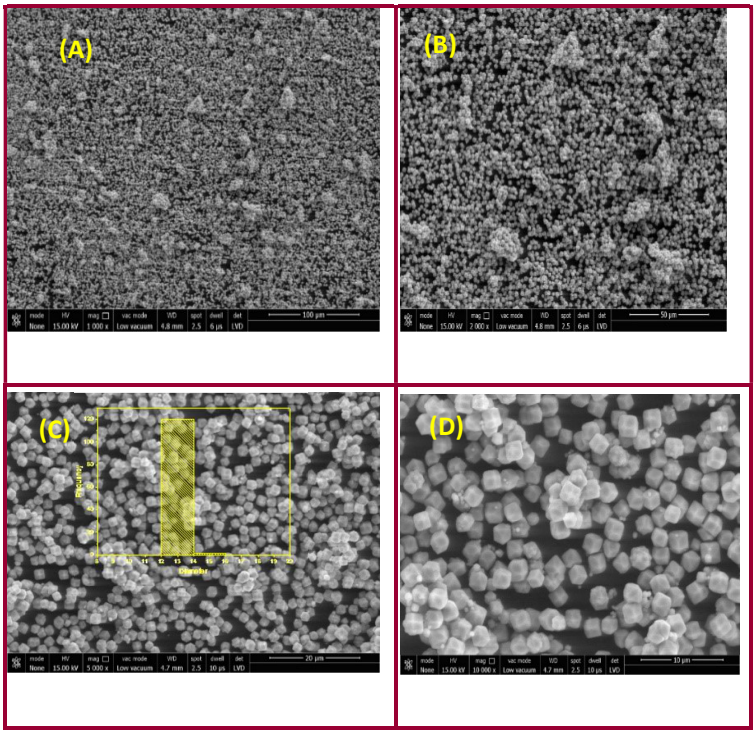

Fig. 2.5 FESEM image with size distribution histogram (inset).

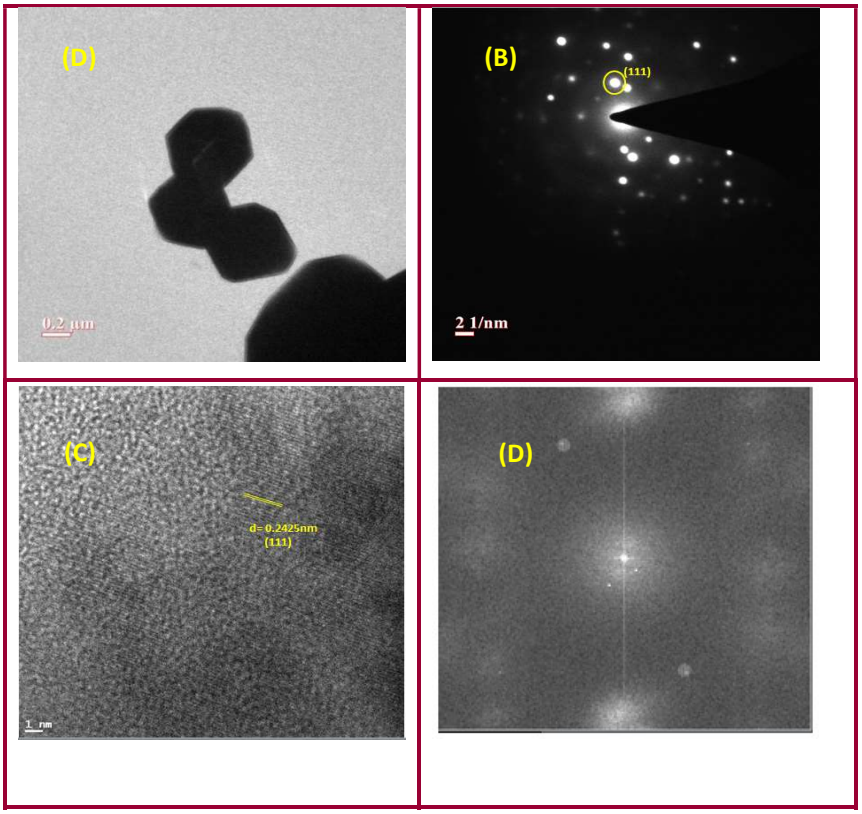

Fig. 2.6 (A) HRTEM image (B) SAED pattern showing intense diffraction from {111} facets(C) lattice fringes with calculated d-spacing of *o*-Cu_2O NCs.

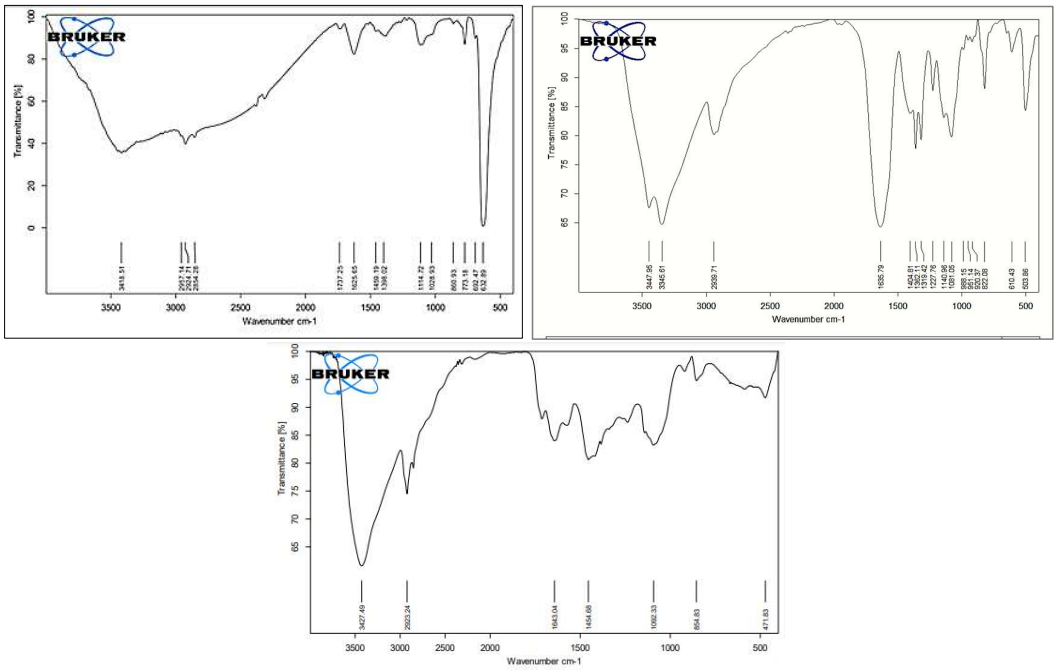

Fig. 2.7 FTIR spectra of *o*-Cu_2O NCs (A) before model oxidation reaction (B) after model oxidation reaction(C)polyvinyl alcohol.

Now, it is obvious to think about the aggregation and stability of NCs in the removal of the CA when suspended in a suitable solvent system for catalysis. Weak interparticle forces like van der Waals interactions, hydrophobic interactions, and electrostatic attractions are mainly responsible for the agglomeration of nanoparticles. Interestingly, it can be observed from Table 2.1 that *o*-Cu_2O NCs float on the surface of the highly nonpolar solvent while getting agglomerated and stick on the inner glass wall of the test tube on increasing the polarity of the solvent (Fig. 2.8). The polarity of the solvent like acetonitrile is the transition point where the NCs can remain suspended for 3 days. These observations suggest that the highly polar solvents like water and alcohols that favour the agglomeration of the particles cannot be useful as solvent systems for the *o*-Cu_2O-mediated organic catalytic transformations. The polarity of the solvent can be tuned to achieve optimum performance. These observations will be further explored during the optimization of reaction parameters. The ξ-potential represents the charge of a particle with respect to the surrounding environment. It represents the charge of the electric double layer produced by the surrounding ions or polar solvent molecules. However, particles with spherical shapes are considered, in most cases, for the calculation. In the case of nanocrystals with a specific facet exposed with one charge, some other facets (in minor quantity) have an opposite charge. Accordingly, the (polar) solvent molecules orient surrounds the surfaces and the particle as a whole. In the present case, the as-synthesized octahedral NCs have eight (111) facets having Cu^{1+} ions with dangling bonds exposed with a bit of depression at the centre. Now, around these surfaces, the solvent molecules orient and make the electric double layer. The literature indicates that nanoparticles systems having surface charges around -28 to -30 mV are stable[17] and can efficiently provide the surfaces required for the catalytic chemical transformation.

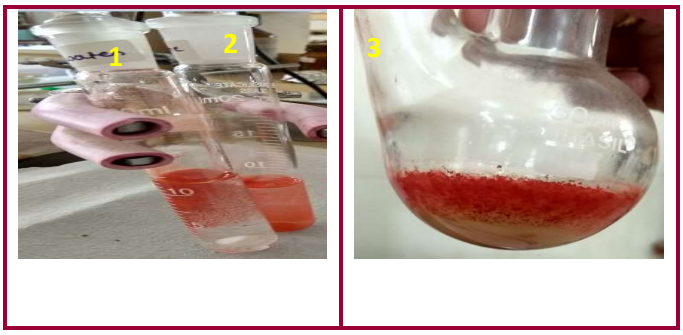

Fig. 2.8 Suspension of *o*-Cu_2O NCs in different solvents. 1. Water: particles adhere on the test tube wall 2. n- Hexane: particles suspended 3. In Acetonitrile: particles adhere to the wall of the reactor.

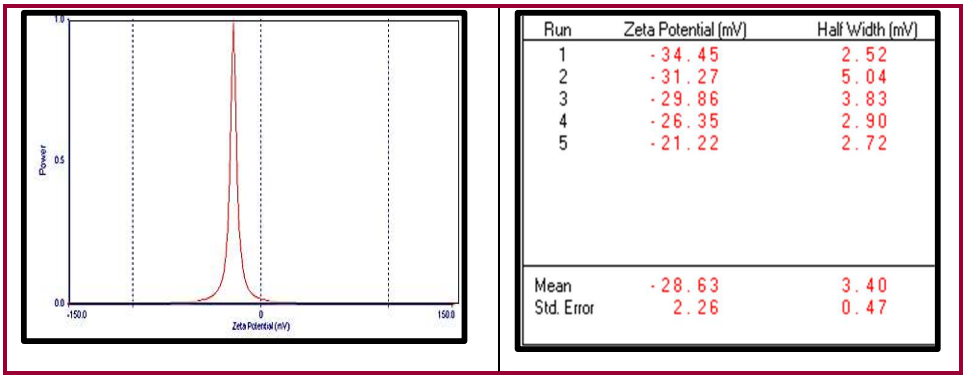

Fig. 2.9. Zeta potential of as-synthesized *o*-Cu2O NCs.

After experimental work-up and removal of the CA, the zeta (ξ) potential of an aqueous solution of *o*-Cu_2O NCs was measured to get insight into the role of surface charge and stability. It can be observed from Fig. 2.9 that the *o*-Cu_2O NCs exhibit an overall -28.63 mV surface charge corresponding to the electrostatically stable system. Hence, on removing the capping agent, the stability of the particles is not affected. Band gap was calculated by tauc plot it was found in visible range (Fig. 2.10).

Table 2.1. Suspension of o-Cu_2O NCs in different solvents according to their order of polarity.

SR No.	Solvent	Polarity	Observation about NCs
1.	Dioxane	0.164	Float on the surface of the solvent
2.	n-Hexane	0.009	Particles remain suspended.
3.	THF	0.207	Float on the surface of the solvent
4.	Dichloroethane	0.269	Float on the surface of the solvent
5.	Acetonitrile	0.460	Remain suspended and adhere to the surface of the glass reactor on the third day
6.	Methanol	0.762	Adhere on the surface of the glass reactor
7.	Ethanol	0.654	Adhere on the surface of the glass reactor
8.	Water	1	Adhere on the surface of the glass reactor

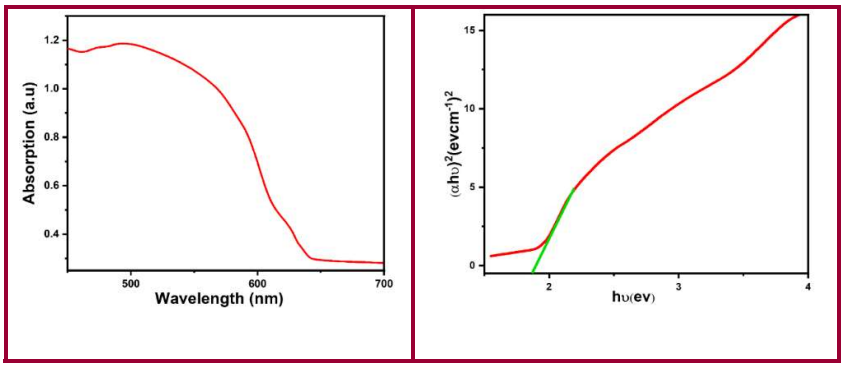

Fig. 2.10 UV-Vis spectra of synthesized NCs.

2.5 Experimental

The synthesized *o*-Cu_2O NCs were used as the catalyst for the benzylic sp^3 C-H oxidation of small organic molecules with a suitable oxidant. Our investigation began with the oxidation of diphenylmethane (DPM; 1) as a model reaction to optimize the reaction parameters (Table 2.2). On a literature survey, we found that Tan et al. carried out the benzylic oxidation of C_{sp3}-H bond to ketone using different oxidants. They obtained maximum yield (91%) for the direct oxygenation of ethylbenzene to acetophenone at 100-130 °C. From examining an array of organic peroxides for this reaction, they found t-butyl hydroperoxide (TBHP) to be the most suitable oxidant.[18] Keeping this in mind, we first started with H_2O_2 (30% solution in water) for the oxidation of benzylic C-H bond of 1 as a substrate in the presence of *o*-Cu_2O NCs as a catalyst in an aqueous medium. In an attempt to optimize the reaction parameters, we fixed the amount of 1 as 1.0 equiv and varied the amount of oxidant accordingly in the presence of maximum catalyst loading (30%). We found that water cannot be used as a solvent even though the magnetic stirring was kept maximum due to solubility issues. Then, we selected the solvent on the basis of polarity order. However, there was no significant improvement in the reaction outcome after 6 days when THF, DCE, 1,4-dioxane, and MeOH were used as solvents. (entries 1, 2, 3 and 4, Table 2.2). We also explored solvent mixtures in different proportions and catalyst loading. It can be observed from Table.2.2 that only 37% yield was achieved at RT in the MeOH/ACN (4:1) mixed solvent system after 2 days, which is extended to a maximum of 41% at the end of the 6th day (entry 7, Table 2.2). On increasing the catalyst loading and temperature in the same solvent mixture system, the reaction yield can be increased to 66 and 78%, respectively (entries 8 and 9, Table 2.2). We also carried out the contrast experiments (entries 11 and 12, Table 2.2); however, however, there was no significant improvement in the yield, and comparatively reduced yield was obtained then in the case of pure acetonitrile. However,

it was observed that the reaction yields improved when carried out under dark conditions or an inert atmosphere. This will be discussed later in detail. Out of all of the solvents and their combination in different proportions (Table 2.2), we found acetonitrile (ACN) as the most suitable for the reactants' solubility. Hence, we selected ACN as a solvent, TBHP as an oxidant, and optimized the other reaction parameters. From all of these experimental results, we found that around 92% yield of 2 with 100% selectivity for carbonyl product was achieved when 1.0 equiv of 1 and 4.0 equiv of TBHP were mixed in the presence of 3.5% Cu_2O at RT, and the reaction mixture was stirred over the magnetic bar for 6 days (entry 15, Table 2.2). Wang et al. developed this kind of reaction for the room-temperature oxidation of heterobenzylic sp^3 C-H bond[19]. we had selected molecular O_2 instead of TBHP as an oxidant keeping other parameters constant; we found that no product was formed although the reaction was continued for 6 days at RT (entry 23, Table 2.2). We had carried out controlled experiments that showed no product was formed in the absence of TBHP or catalyst (entries 19 and 20 in Table 2.2). From these experiments, it can be concluded that aerial oxidation of benzylic C_{sp3}-H bond in the presence of *o*-Cu_2O NCs without TBHP does not occur. During optimization of reaction parameters, when the model reaction was carried out in the aerial atmosphere and ACN as a solvent at RT, we observed that (1) the solvent shows a greenish-blue tint after 48 h and the color deepens with time; (2) the solid catalyst particles firmly adhere on the wall of the glass reactor and form a thin circular layer instead of forming a suspension in ACN after 72 h depending on the polarity of the solvent; (3) the red catalyst layer becomes thinner on the wall of the glass reactor with time; (4) after 96 h, the residues of the red catalyst remain on the wall of the glass reactor, while light blue solid particles get settled at the bottom with a clear transparent blue solution with complete oxidation of 1 (Fig. 2.11 A,B).

Table 2.2. Optimization of Reaction parameters.

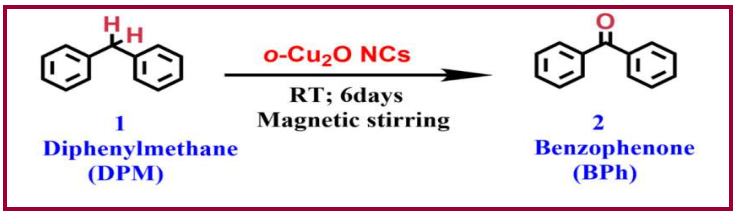

Entry	Oxidant	1/TBHP/*o*-Cu_2O	Solvent	Yield[a] %
1.	TBHP	1:4:3.5	THF	19.29
2.	TBHP	1:4:3.5	Dichloroethane	42.20
3.	TBHP	1:4:3.5	Methanol	49.80
4.	TBHP	1:4:3.5	1,4-Dioxane	30.30
5.	TBHP	1:2.5:20	MeOH:CH_3CN (4:1)	34
6.	TBHP	1:4:20	MeOH:CH_3CN (4:1)	21.59
7.	TBHP	1:4:25	MeOH:CH_3CN (4:1)	40.59
8.	TBHP	1:4:30	MeOH:CH_3CN (4:1)	65.69[b]
9.	TBHP	1:4:30	MeOH:CH_3CN (4:1)	78.29
10.	TBHP	1:4:3.5	MeOH:CH_3CN (4:1)	87[c]
11.	TBHP	1:4:3.5	Water	NR
12.	TBHP	1:3:3	CH_3CN	60
13.	TBHP	1:4:3.5	CH_3CN	92
14.	TBHP	1:6:3.5	CH_3CN	89.86
15.	TBHP	1:5:5.9	CH_3CN	89.02
16.	TBHP	1:6:5.9	CH_3CN	91.60
17.	---	1:---:3.5	CH_3CN	NR
18.	TBHP	1:4:----	CH_3CN	NR
19.	TBHP	---:6:5.9	CH_3CN	NR
20.	O_2	1:----:3.5	CH_3CN	NR
21.	TBHP	1:6:5.9	CH_3CN	91.60[d]

[a]Isolated yield. [b] Reaction was carried out at 52°C. [c] Reaction was carried out in dark.[d] Reaction was carried out under N_2 atm.

The progress of the reaction was monitored on the TLC plate using benzophenone and benzhydrol (CAS No. 91-01-0) as standards throughout this period; and (5) at the end of the 6th day, the red layer on the glass wall is either wholly removed, forming light blue powder at the bottom with a clear colourless solution or remains completely adhered with the glass wall

with no color change of the solution depending on the reaction conditions and varies from the substrate to substrate discussed later.

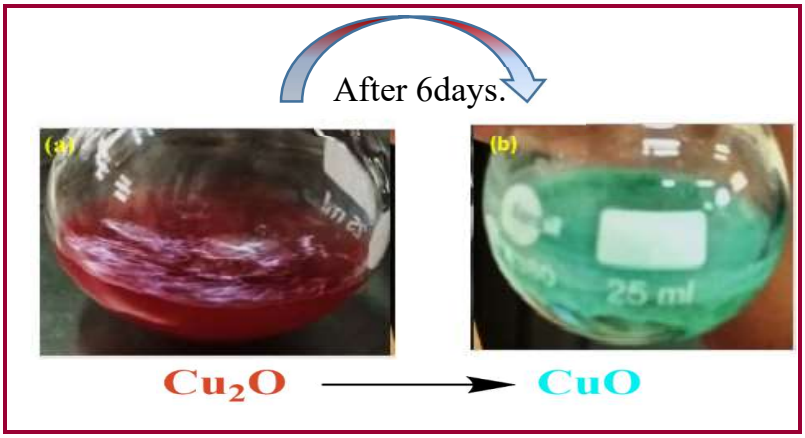

Fig. 2.11 Fate of the model reaction carried out in presence of as-synthesized *o*-Cu_2O NCs (a) on the 1st day and (b) on the 6thday.

X-ray photoelectron spectroscopy analysis (XPS) of both samples (the glass surface adhered powder and the light blue powder settled at the bottom of the reaction mixture) was carried out to find the oxidation state of the copper ions. The survey XPS spectrum and the deconvoluted (Gaussian) XPS profiles of Cu 2p and O 1s are presented in Fig. 2.12 and Fig. 2.13. From the survey spectrums, the presence of Cu and O as sole elements confirms the purity of the material. Two strong peaks for Cu $2p_{3/2}$ appear at 932.2 and 933.5 eV in the deconvoluted spectrum (Fig. 2.13 A), which can be assigned to closed d^{10} (Cu^{+1}) and open d^9 (Cu^{2+}) orbitals, respectively, having 1 eV difference in binding energy. The shake-up satellite peaks at 940.3 and 943.1 eV are the signatures of open $3d^9$ shell in a in a ground state corresponding to Cu^{2+} ions. The peak at 952.3 eV is the corresponding spin-orbit splitting ($2p_{1/2}$) of Cu_2O. Hence, it can be established that the sample is made of mainly Cu_2O core.[20] From the deconvoluted XPS spectrum of the recovered powder after six days of reaction (Fig. 2.13 C), the strong peak at 935 eV and consecutive satellite peaks at 943 and 944 eV, also strong $2p_{1/2}$ peak at 952.3eV confirm CuO. The deconvoluted O1s spectra are displayed in Figure 2.13 B and 2.13 D. The binding energies 529.5 and 530.2 eV are due to CuO and Cu_2O, respectively. In Cu_2O (Fig. 2.13 B), a shoulder at about 1.8 eV higher binding energy from the prominent peak is due to surface adsorbed oxygen.[21]The XPS survey spectrum of Cu_2O shows the atomic percentages of Cu and O estimated as 83.09 and 16.91% and that of CuO, 55.48 and 44.52%, respectively (Fig. 2.12 a and b), also corroborated from the deconvolution results (Table 2.3). These observations suggest surface-initiated oxidation of Cu_2O to CuO with time in six days under the optimized conditions. From these observations, it can be predicted that oxidative

obliteration of the catalyst Cu_2O to CuO (Reaction 2) occurs concurrently with the oxidation of benzylic sp^3 C-H to ketone (Reaction 1) in the presence of air. When the same experiment was carried out in N_2 atmosphere under the optimized reaction parameters product **2** formed with the same %yield without scarification of the catalyst in a specified time (entry 24, Table 2.2). Hence, we believed that Reaction 2 is due to Cu (I) aerial oxidation to Cu (II).

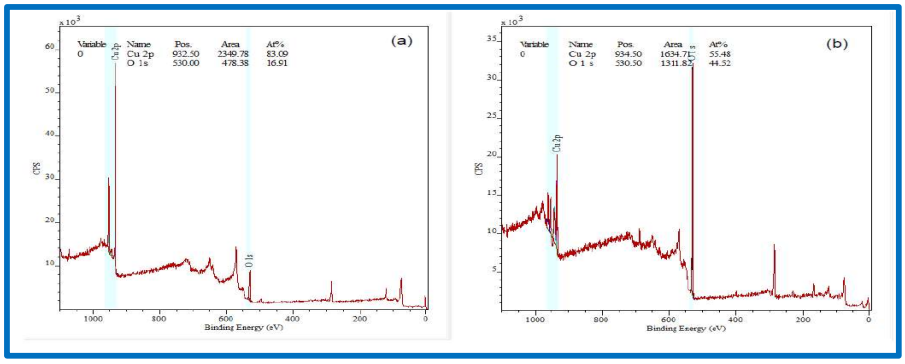

Fig. 2.12 Core level XPS of the *o*-Cu_2O- Survey spectra.

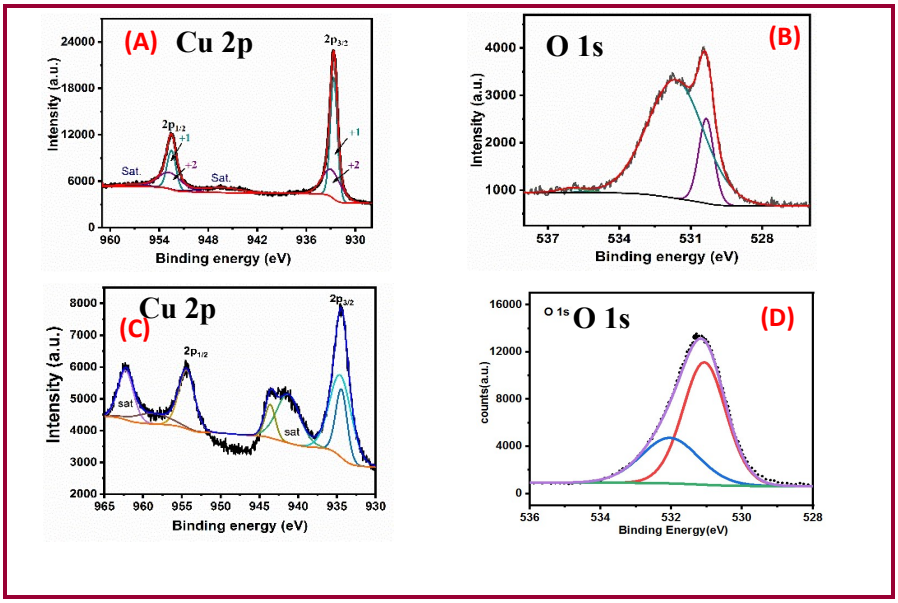

Fig. 2.13 The deconvoluted XPS of (A) Cu $2p_{3/2}$ and Cu $2p_{1/2}$ of Cu_2O NCs (B) O 1s spectra of Cu_2O NCs (C) Cu $2p_{3/2}$ and Cu $2p_{1/2}$ of CuO NCs (D) O 1s spectra of CuO NCs.

Table 2.3 The deconvolution results of XPS.

	Binding energy of Cu $2p_{3/2}$ (eV)	Phase	FWHM	Area	Atomic %
Fig. 4a	932.64	Cu_2O	0.997	16526.77	36.16
	932.86	Cu_2O	2.530	10657.71	23.32
	946.42	Cu_2O	4.964	3161.62	6.92
Fig.4b	Binding energy of O1s(eV)	Phase	FWHM	Area	Atomic %
	530.35	Cu_2O	0.763	1499.49	16.55
	531.66	Chemisorbed oxygen/ hydroxide	2.791	7558.45	83.45
	Binding energy of Cu $2p_{3/2}$ (eV)	**Phase**	**FWHM**	**Area**	**Atomic %**
Fig. 4c	934.42	CuO	1.752	4031.43	12.86
	934.53	CuO	3.248	9017.07	28.76
	941.36	CuO	3.706	6141.62	19.58
	943.64	CuO	1.421	1464.55	4.67
Fig. 4d	Binding energy of O1s(eV)	Phase	FWHM	Area	Atomic %
	531.06	CuO	1.348	11226.40	44.59
	531.62	CuO	2.228	13950.42	55.41

It is obvious to question the catalytic effect on Reaction I due to the Cu_2O NCs or CuO in the reaction mixture. We carried out one model oxidation reaction in the presence of commercial CuO under optimized reaction conditions (under aerial atmosphere and in the presence of light). We obtained a very major yield (almost 20%) at the end of the fourth day of reaction. It may be due to the defects and vacancies in the material. This discussion is out of the scope of this work. As the synthesized compound was characterized by elemental analysis, powder XRD, and XPS analysis, it confirms that the Cu_2O NCs are responsible for the catalytic activity. For further insights into the role of catalyst, it is necessary to understand the nature of oxidation reaction. Literature survey reveals that Reaction I takes place in multiple steps and mediated by free radicals or ROSs (Scheme 2.8).

The protocol developed by Tan et al. requires the high temperature for the homolytic cleavage of peroxide bond to generate reactive free radical species (·OH and ^{t}BuO·)[18]. These ROSs abstract the H· of the benzylic sp^3 C-H bond leads to the product **2**. The (111) facets of Cu_2O octahedra expose positive Cu (I) ions with dangling bonds, attract TBHP molecules on their surface. Theoretical calculations show that -O-O- homolytic bond cleavage becomes barrier-less on such surfaces.[22]The hydroxyl free radicals produced then generate secondary reactive species like $O_2^{\cdot-}$, ·OOH, etc. on reaction with aerial oxygen. Hence, it can be assumed that *in situ* generated ·OH free radicals attack on **1** as a substrate as well as formed the secondary ROSs on reaction with aerial O_2. The superoxide radicals $O_2^{\cdot-}$ may be responsible for the oxidation of Cu (I) to Cu (II).

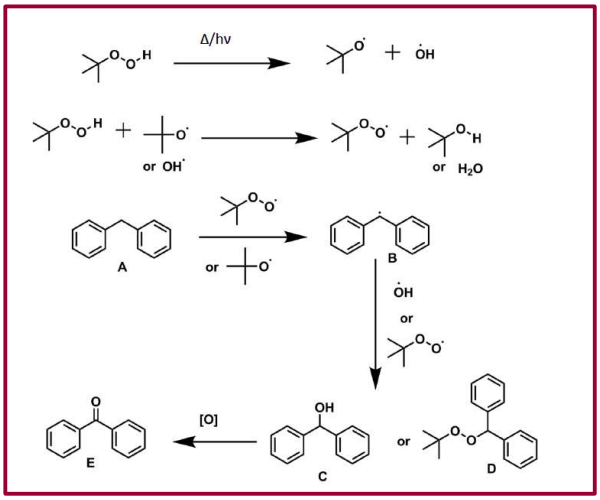

Scheme 2.8 Traditional mechanism of free radicals mediated oxidation of benzylic sp^3 C-H bond.

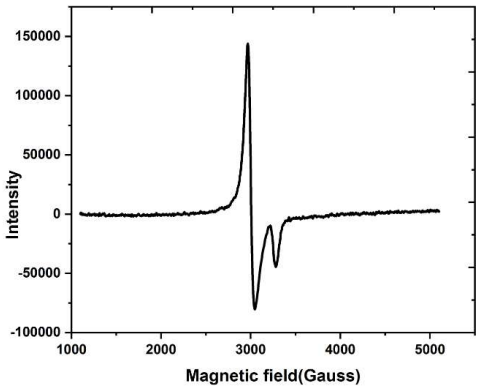

Fig. 2.14 ESR spectra of reaction mixture after two days of reaction at low temperature.

Electron Paramagnetic Resonance (EPR) measurements can provide information on ROSs involved during the reaction. The ESR of the reaction mixture after 48h was carried out (Fig. 2.14), confirming the presence of Cu^{2+} ions in an axial environment in the solution ($g_{\perp} = 2.21$, $g_{\parallel}=2.05$), but ESR is "silent" about Cu^{1+} ions. The ESR analysis of the reaction mixture with TEMPO was also carried out. However, any ROSs adduct could not be detected. It may be due to short-life time and cascade of reactions taking place on the surface of the *o*-Cu_2O NCs. According to Huang et al., this technique does not provide information about the number of photogenerated electrons and holes to reach the crystal surface. Also, it requires expertise to analyze the results.[23] Indirect techniques involving e^-, h^+, and ROSs scavengers are more convenient and insightful. Hence, to find out which ROSs is involved in the transformation of

the benzylic C_{sp3}-H bond to ketone and parallel oxidation of Cu(I) to Cu(II), the model experiments involving free radical scavengers were carried out (Table 2.4).

Table 2.4 Scavenger experiments carried out to detect the ROS involved during the reaction.

Sr.No.	Scavenger	ROSs	Reaction I 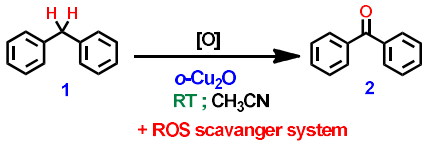	Reaction II 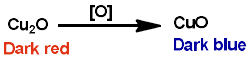
1	Isopropyl alcohol (0.01 M)	·OH	Complete conversion with 100% selectivity on the fourth day of the reaction.	Starts on third day with residual Cu_2O on the wall of the reactor.
2	KI (0.01 M)	Surface adsorbed ·OH or ^{+}h	Complete conversion with 100% selectivity on the fourth day of the reaction.	Starts on third day with residual Cu_2O on the wall of the reactor.
3	$KBrO_3$ (0.01 M)	e^-	90% yield	No reaction
4	$KBrO_3$ (0.01 M) + KI (0.01 M)	$e^- + {}^{+}h$	90% yield	No reaction
5	Ascorbic acid (30 mM)	$O_2^{\cdot-}$	60% yield	No reaction
6	Benzoquinone (30 mM)	$O_2^{\cdot-}/HO_2^{\cdot}$	60% yield	No reaction
7	Isopropyl alcohol (30 mM) + benzoquinone (30 mM)	$HO^{\cdot}$ + $O_2^{\cdot-}/HO_2^{\cdot}$	60% yield	No reaction

When isopropyl alcohol was used as ·OH scavenger, a complete conversion of **1** to **2** on the fourth day with total catalyst obliteration on the sixth day was observed (entry 1, Table 2). Hence, hydroxyl free radicals are not responsible for both reactions. Initially, we assumed that superoxide anionic free radical should be accountable for both the oxidation processes. However, it was established that the $O_2^{\cdot-}$ radicals are not that 'super' to carry out the oxidation of **1** to **2**,[24] but they got very well solvated and solubilized in the solvent, particularly ACN. We

carried out more controlled experiments to determine the species responsible for oxidation processes (Table 2.4 and 2.5, Fig. 2.15).

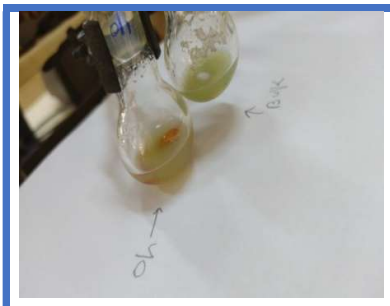

Reaction in presence of bulk and o-Cu_2O NCs.

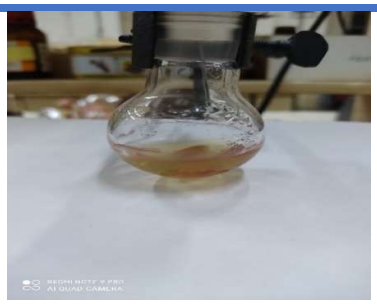

Reaction under oxygen atmosphere

Reaction under nitrogen

Reaction under nitrogen atmosphere (on sixth day).

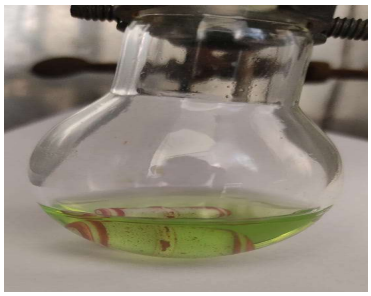

atmosphere (on first Day).

Reaction in dark

Reaction of 4-benzylphenol

Fig.2.15 Model oxidation reaction under special conditions.

It can be concluded from these experiments that (i) $^{\bullet}OH$ is not required for both the processes (entry 1, Table 2.4) (ii) surface adsorbed $^{\bullet}OH$ cannot oxidize Cu (I) to Cu (II) (entry 2, Table 2.4) (iii) as Cu_2O is a p-type semiconductor, e_{CB}^{-} and h_{VB}^{+} are produced in the presence of light. Huang et al. explained that these charge carriers could easily transfer to the adsorbed species on the (111) facets of octahedra due to less band bending.[25] Hence, the surface adsorbed oxygen should be converted into $O_2^{\bullet-}$ by e_{CB}^{-}. But it is easily solvated in ACN. So, it is a weak oxidant

and cannot oxidize **1** to **2** but responsible for Reaction 2 (entry 3, 4, Table 2.4) (iv) in the dark, $O_2^{\cdot-}$ cannot be produced (entry 1, Table 2.5) (v) if the reaction was carried out under N_2 atmosphere, the Reaction 1 takes place, but Reaction 2 could not due to the absence of oxygen/ $O_2^{\cdot-}$ (entry 2, Table 2.5). Hence, it can be observed that the formation of $O_2^{\cdot-}$ is the primary requirement for Cu (I) to Cu (II) oxidation. However, it cannot be involved directly in the reaction. Here, we propose the superoxide free radical get disproportionate in the manner shown in equations 1 -3.

$$HO^{\cdot} + HO^{\cdot} \rightarrow \quad H_2O_2 \qquad (1)$$

$$H_2O_2 + \ O_2^{\cdot-} \rightarrow HO^{\cdot} + O_2 + HO^{-} \qquad (2)$$

$$H_2O_2 + h_{VB}^{+} + HO^{-} \rightarrow HO_2^{\cdot} + \ H_2O \qquad (3)$$

$HO_2^{\cdot}$is a strong oxidant compared to $O_2^{\cdot-}$ responsible for Cu(I) oxidation.[26] Hence, light (in normal laboratory conditions and not irradiated from any lamp of a specific wavelength), TBHP, and aerial oxygen are the pre-requisites for both processes.

Table 2.5 Special experiments carried out to evaluate the reaction pathway.

Sr. No.	Special Conditions	Reaction I 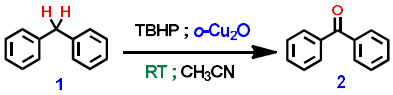	Reaction II 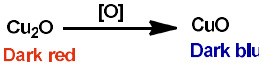
1	Reaction in dark	90% yield	No reaction
2	Reaction under N_2 atmosphere	90% yield	No reaction
3	Reaction under N_2 atmosphere + 5 mL IPA	No reaction	No reaction
4	Reaction under O_2 atmosphere	90% yield	No reaction.
5	Reaction under O_2 atmosphere and No TBHP	No reaction	No reaction
6	Reaction under air flow	92% yield	Complete colour change on sixth day.
7	In absence of **1**	-	No reaction

It is pretty obvious to think about the involvement of $HO^{\cdot}$ free radicals and oxidation of benzylic sp^3 C-H in two steps via benzylhydrol (**3**) as an intermediate (Scheme 2.9). However, we did not find any evidence of it on the TLC plate compared with the standard compound (CAS No. 91-01-0) or mass spectrogram (Fig. 2.16).

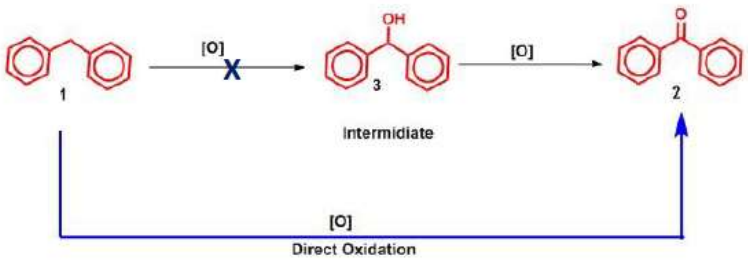

Scheme 2.9 Benzylic Csp3-H oxidation of diphenylmethane (1) and benzhyldrol (3) to benzophenone (2) on the (111) facets of *o*-Cu_2O NCs.

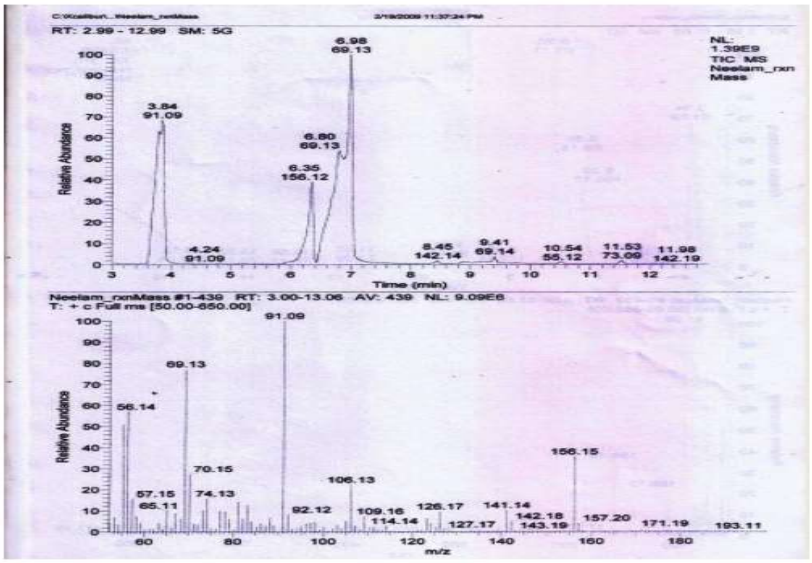

Fig. 2.16 Mass spectrogram of reaction mixture having ethylbenzene as a substrate under the optimized reaction conditions.

This was also confirmed when the reaction was carried out in the presence of IPA as $HO^{\cdot}$ scavenger, which resulted in the final carbonyl product formation at the end of fourth day of the modal reaction under the optimized conditions with the complete colour change of the catalyst on the sixth day (entry 1, Table 2.4).

Interestingly, when the model reaction was carried out under N_2 atmosphere in the presence of 5 mL of IPA, no product was formed. At the same time, the catalyst remained unaffected at the end of the sixth day (entry 3, Table 2.5). It can be observed from Table 2.5 (entry 2) that the reaction under the N_2 atmosphere yields the final carbonyl product, which begins to form from the second day of the reaction without any color change of the catalyst. This observation leads to believe the involvement of O_2^{-} as ROS and the way by which the reaction proceeds which is

discussed later. Further, the complete success of Reaction 1 in the presence of KI, eliminates the possibility of involvement of any surface adsorbed $HO^{\cdot}$ or h_{VB}^{+} in the reaction,[27] (entry 2, Table 2.4). Interestingly, when this reaction was carried out in sunlight and $KBrO_3$ there was no color change of the catalyst, but the product was formed (entry 3, Table 2.4), [28] and similar observation in the dark without $KBrO_3$ (entry 1, Table 2.5). This indicates the transfer of electrons (a SET mechanism) from the semiconductor surface to the adsorbate in the presence of light.[29] Ascorbic acid (AA) and benzoquinone (BQ) are known $O_2^{\cdot-}$ scavengers. Separate experiments were carried out in the presence of AA and BQ, indicated that the carbonyl product was formed with almost 60% yield, but the oxidation of catalyst did not take place (red color remains intact). Similar observation with the experiments carried out in both AA/BQ and IPA in excess (30 mM) (entry 5, 6, and 7, Table 2.4). These observations suggest (1) no $O_2^{\cdot-}$ or $HO^{\cdot}$ are directly involved in the benzylic oxidation of sp^3 C-H bond (2) the oxidation of Cu(I) to Cu(II) takes place through the generation of $O_2^{\cdot-}$ in the presence of light and surface adsorbed O_2 (3) catalyst alone is not able to break O-O bond of TBHP (entry 7, Table2.5) (4) the mode of breaking of O-O bond is governed by surface adsorbed reactant molecules as well as the presence of aerial oxygen and light. Intuitively, to decrease the reaction time and introduce the green aspect, we carried out the reaction in an O_2 atmosphere (entry 4, Table 2.5). We observed that the product is formed within 48 h, but surprisingly, the red color of the catalyst remains for seven days, indicating complete surface passivation by O_2 molecules preventing further oxidation and annihilation of the catalyst.

Further, we carried out the model reaction with pure O_2 as an oxidant instead of TBHP under optimized conditions (entry 5, Table 2.5). However, the reaction did not proceed till it was continued for six days, suggesting the necessity of TBHP as an oxidizing agent. The same was observed when a stoichiometric amount of H_2O was used instead of TBHP under the optimized reaction conditions (entry 11, Table 2.2).

By compiling all the above experimental observations, we propose the mechanism for both the processes shown in Scheme 2.10 and 2.11.

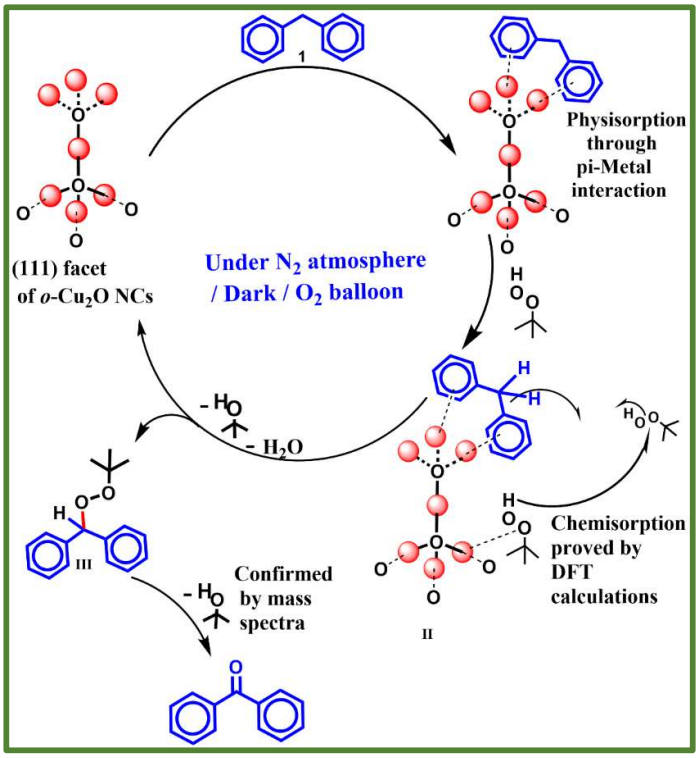

Scheme 2.10 Proposed reaction mechanism for benzylic sp^3 C-H oxidation of 1 with TBHP in presence of *o*-Cu_2O NCs under N_2 atmosphere/aerial atmosphere under dark condition/O_2 balloon. Orange balls indicate Cu^{1+} ions.

It can be observed from Scheme 1 that DPM (**1**) gets physisorbed on the catalyst (111) surface with Cu^{1+} ions through pi-metal interactions, in turn, TBHP also chemisorbed on the surface, resulting in the cascade of the chemical reactions. The peroxo intermediate (III, Scheme 2.10) forms at the end, desorbed from the surface, and decomposed into the carbonyl product, vacating the catalyst surface for the next cycle under N_2 atmosphere or aerial atmosphere in the dark condition or under the flow of oxygen gas. Now, under the normal aerial condition and in the presence of light (day-light and from Hg CFL tubes in the laboratory at night), the aerial oxygen chemisorbed on the Cu_2O (111) surface and get activated by a single electron transfer (SET) mechanism resulting into end-on η1-superoxo species (A).[30,31] This chemisorbed and activated Cu(II)-superoxide, in turn, abstract ·H from the peroxide intermediate (III),[32] disintegrating into the carbonyl product. However, the resulting end-on, η^1 -hydroperoxide (B, HOO-Cu^{II}) and t-butoxide ($(CH_3)_3O$-Cu^{II}, presence of which on the surface has been confirmed by mass spectra, Figure 2.2.14) species on the surface undergo a cascade of chemical events forming μ-1,2-peroxo-Cu_2^{II} adduct **C** on the surface. This, in turn, undergoes internal electron transfer and complete lattice restructuring resulting in $Cu^{II}O$ powder (D,

Scheme 2.11). The CuO can be recycled to (111) facets of o-Cu_2O by careful ascorbic acid treatment When 4-benzylphenol (**5**) was oxidized under optimized reaction conditions (Scheme 2.12), we did not obtain the carbonyl product at the end of the sixth day.

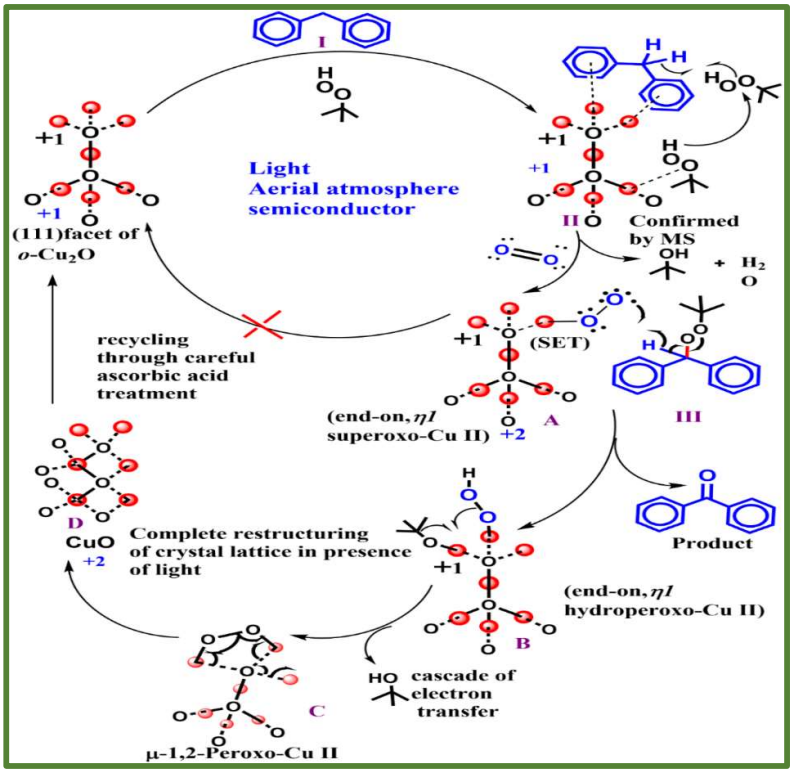

Scheme 2.11 Proposed reaction mechanism of benzylic sp^3 C-H oxidation of 1 with TBHP in presence of *o*-Cu_2O NCs in aerial atmosphere and light. Orange balls indicate Cu^{1+} ions.

However, the peroxide product **6** was formed (confirmed by ^{1}H NMR spectroscopy) without catalyst annihilation (Fig. 2.15), strengthening our argument about the presence of t-butoxide radical on the surface (Fig. 2.16) and its role during Reaction II.

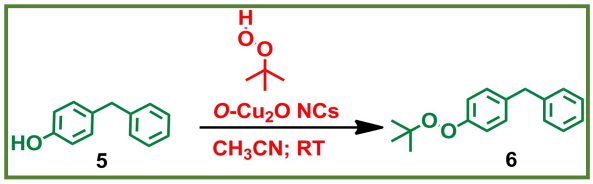

Scheme 2.12 Oxidation of 4-benzylphenol (5) to the peroxide product (6) in the presence of *o*-Cu_2O NCs under the optimized reaction conditions.

Further, to ensure the peroxide exchange and not the carbonyl product formation, the reaction mixture was treated with sodium metabisulphite for six days, resulted in the decomposition of **6** into **5.** To support the proposed reaction mechanism, electrochemical analyses of the synthesized *o*-Cu_2O NCs were carried out. Mott-Schottky analysis is considered an effective method to measure the carrier density and flat band potential of the *o*-Cu_2O NCs. The Mott-Schottky plot of as-synthesized *o*-Cu_2O NCs, within the potential range of 1.0 to 2.5 V, shows the negative slope confirming the p-type semiconductor behaviour (Fig. 2.17).[33]

The acceptor density (N_A) was calculated by using the equation [34]

$$N_A = 2/e\varepsilon\varepsilon_0 * (\text{slope}) \qquad (4)$$

where e, ε, ε_0 and N_A are the electron charge (1.602×10^{-19} C), dielectric constant (7.60 for Cu_2O), permittivity of the vacuum (8.85×10^{-14} F cm^{-1}) and acceptor density (hole density in p-type Cu_2O), respectively (Table 2.6). [35]

Table 2.6 Conductivity and Mott-Schottky parameters of *o*-Cu_2O NCs.

Sample	Conductivity (mS cm^{-1}) Under dark	Conductivity (mS cm^{-1}) Under light	Slope[b]	Acceptor density[b] (N_A)
o-Cu_2O	3.08×10^{-4}	7.42×10^{-4}	-7.29 X 10^{11}	2.55 X 10^{19}

Parameters calculated from [a]EIS and [b]Mott-Schottky plots.

The EIS measurements for the electronic activity of the *o*-Cu_2O NCs in presence and absence of light during organic transformation are performed at a bias potential of 10 mV under sinusoidal ac frequency (1.2 MHz to 0.1 Hz), and the corresponding imaginary Z″ vs real Z′ plots (Nyquist plots) are shown in Fig. 2.17 A. The equivalent circuit used to fit the curve is shown in Fig. 2.17 B. Each component in the circuit specifies the specific electrochemical processes at the electrode material and the electrolyte interface at different frequency regions. The R represents the charge transfer resistance in the equivalent circuit and is associated with the conductivity difference between the electrode and electrolyte. The C component in the equivalent circuit represents the non-faradic charge separation at the interface between the working electrode, and the electrolyte is considered a double-layer capacitor. The conductivity was calculated using eq 6, which indicates that the *o*-Cu_2O NCs possess a low conductivity of 3.08 x 10^{-4} mS cm^{-1} in the dark condition, while an increase in the overall conductivity to 7.42 x 10^{-4} mS cm^{-1} noted in the presence of light (Table 2.6). This increase in conductance indicates higher charge transfer with less resistance on the (111) surfaces of the material in the presence

of light responsible for the photocatalytic activities. Cyclic voltammetry (CV) of the catalyst, in light and dark and the presence and absence of substrate (**1**) with TBHP, across the potential range of -1.3 to 1.5 V, was carried out to understand the reaction mechanism (Fig. 2.17). The complete redox cyclic behavior of *o*-Cu_2O NCs can be observed from the CV profile. However, higher order of current observed under the irradiation of light demonstrates the higher redox event within the sample. Therefore, the higher current observed under the light illumination supports the observation about the high photocatalytic activity of the NCs. On addition of **1**, a minimal increment in the current magnitude detected in the dark as well as in light irradiation suggests no significant improvement of the photocatalytic activity of the *o*-Cu_2O NCs on physisorption of **1**. However, the highest order of current detected after the addition of TBHP, indicating the increased photocatalytic activity and confirming the proposed SET mechanism in the presence of light. Moreover, the significant current increment observed on irradiation of light yielding a high conversion rate.

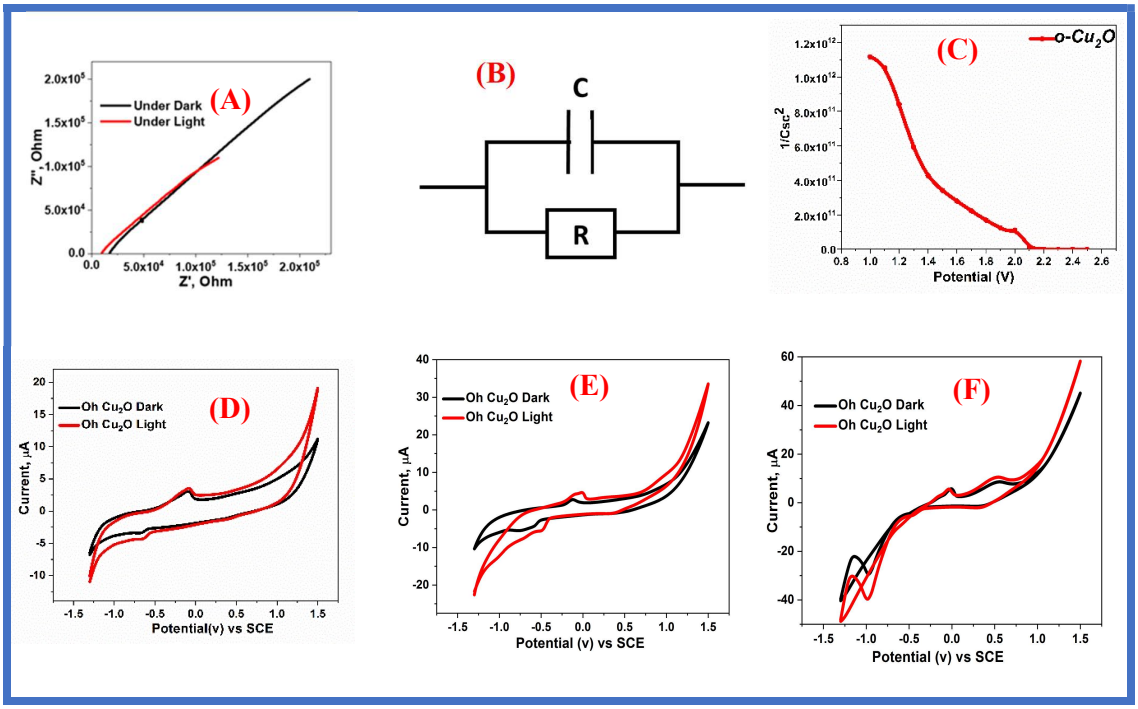

Fig. 2.17 Electrochemical analysis of *o*-Cu_2O NCs. (A) EIS Nyquist plot (B) corresponding equivalent fitting circuit diagram (C) Mott-Schottky plot. Cyclic voltammetry profiles of (D) blank *o*-Cu_2O NCs (E) *o*-Cu_2O NCs with DPM and (F) *o*-Cu_2O with DPM and TBHP in presence and absence of light.

2.6 Structural properties of Cu_2O (111) surface simulated by DFT.

The top and side views of the Cu_2O (111) surface's optimized structure are shown in Fig. 2.18 A, along with the computed bond parameters and angle after relaxation. From Fig. 2.18 A, it can be seen that the Cu planes parallel to the (111) surface contain four Cu^{1+}cations per surface unit cell. Each Cu plane is sandwiched between two O planes, and each of these O planes has one anion per surface unit cell. To generate the Cu_2O (111) surface, the lattice parameter for the unit cell of (111) facets obtained from the optimized values calculated for bulk Cu_2O, i.e., 4.21 Å, with the similar set of above mentioned computational parameters and is in close agreement with the previous theoretical and experimental report.[36]

Adsorption Energetics. To measure the strength of the interaction between the adsorbent (catalyst) and the substrate, the adsorption energy (E_{ads}) is calculated using the following equation,

$$E_{ads} = E_{(substrate+adsorbent)} - E_{(substrate)} - E_{(adsorbent)} \quad (5)$$

where, $E_{(substrate+adsorbate)}$ is the total energy of the adsorbed system. $E_{(adsorbent)}$ and $E_{(substrate)}$ are the total energies of the clean surface and molecule in the gas phase, respectively. The oxygen (O_2) and TBHP adsorbed Cu_2O (111) surface are presented in Fig. 2.18 B and C. The calculated adsorption energy for O_2 and TBHP, along with the bond parameters and corresponding angle, are depicted in Table 2.7. It can be observed from Fig. 2.18 B that O_2 gets chemisorbed on Cu_2O (111) surface by an end-on mode at the angle of 119^o forming end-on, η^1-superoxo-Cu^{II} adduct supports the proposed reaction mechanism in Scheme 2.11. To investigate the interaction mechanism of the TBHP and DPM with Cu_2O (111) surface, their different orientations were explored. In the case of the TBHP, the most favorable adsorption configuration is presented in Fig. 2.18 C. It can be observed that the binding energy decreases (-1.31 eV) when carbon attached oxygen atom of the TBHP and the surface Cu^{1+} ions interact by chemisorption way. In contrast to this, the physisorption between DPM and Cu_2O (111) surface was detected. Other structural parameters are presented in Table 2.7. On observing the proposed mechanism, it can be said that the (111) surfaces of the *o*-Cu_2O NCs mimic the oxygenase enzymes (e.g. particulate methane monooxygenase (pMMO)) activity. It exploits aerial O_2 to oxidize C-H bond of simple hydrocarbon molecules (like methane) to alcohol in biological processes.[37] However, the amino acid residues attached as ligand with catalytic metal centre of enzyme and hydrophobic environment of the enzymatic cavity stabilize the metal-O_2 adduct. They also help the metallic centre back and forth of the oxidation states

without collapsing it completely,[38] which is missed in o-Cu2O (111) surfaces under normal aerial conditions resulting in oxidation of the catalyst to CuO. However, under the flow of oxygen/aerial atmosphere in the dark/inert atmosphere, this activity can be achieved, leading to the carbonyl product to extend the scope of the reaction, we selected various aromatic substrates having benzylic sp^3 C-H bonds and other small hydrocarbon molecules. It can be observed from Table 2.9 that the developed protocol is equally applicable to the substrates having electron-rich C-H bonds, which can be achieved by substituting the electron releasing group to the aromatic ring.[39]

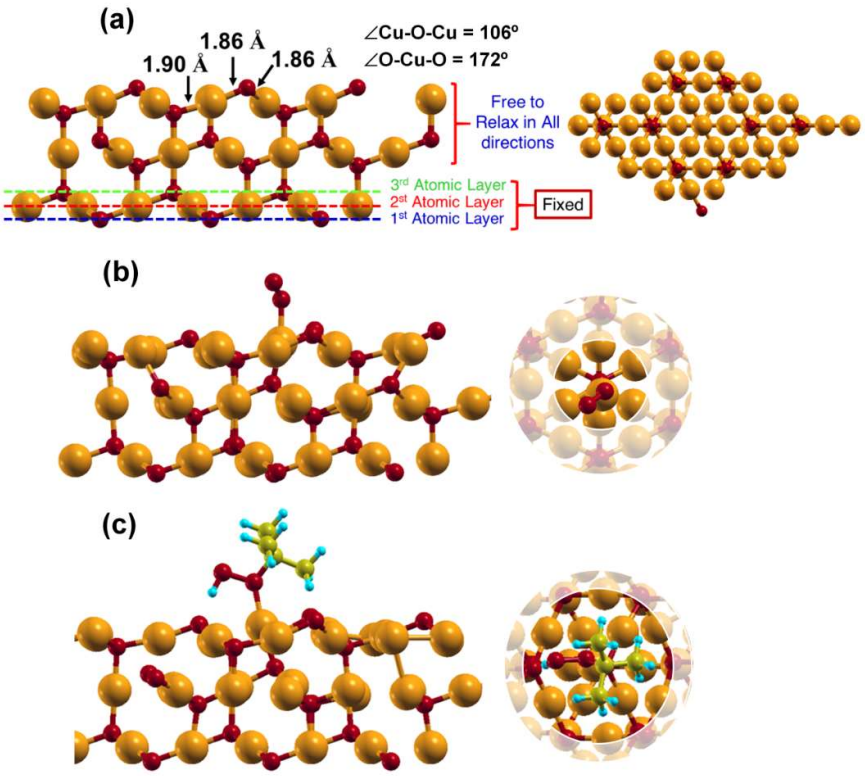

Fig. 2.18 (a) The side and top view optimized atomic model of 3 × 3 Cu_2O(111) surface (b) The side and top view of the adsorbed O_2 over Cu_2O(111) surface (c) The side and top view of the adsorbed tertiary butoxide hydroperoxide (TBHP) over Cu_2O(111) surface. The dark yellow, red, light green and cyan color balls represent the copper, oxygen, carbon and hydrogen atom respectively.

Table 2.7 Adsorption energy (E_{ads}, eV), bond parameters (R_{O-O} (Å) and R_{Cu-O} (Å) and angle (angle Cu – O - O).

Species	E_{ads} eV	R_{O-O} Å	R_{Cu-O} Å	∠Cu-O-O
O_2	-1.50	1.26	1.97	119 °
TBHP	-1.31	1.47	2.01	-

Also, to those C-H bonds which have bond dissociation energies less than 90 kcal/mol.[40] The specialty of this protocol is that it converts the benzylic C-H bond directly to carbonyl without forming any intermediate hydroxyl derivatives. However, it is also applicable for the transformation of benzylic C-OH to carbonyl with the same substrate selectivity. Mimic of oxygenase activity shown by *o*-Cu_2O NCs is an inherent property depicted by p-type semiconductors. Does it bestow due to the exposure of specific facets in excess (facet selective catalysis) or the larger surface area at the Nano regime? To answer this question, BET surface area measurement was carried out for *o*-Cu_2O NCs, found to be 0.057 m^2/g significantly less compared to the conventional nanomaterial used as catalyst (Table 2.8, Fig 2.19). This is the characteristic of exposure of specific facets of a crystal in excess.[41] The same model experiment was carried out in the presence of bulk Cu_2O. We found significantly less yield (40%) at the end of the sixth day with incomplete oxidation of the catalyst, suggesting random surfaces.

Table 2.8 BET surface characterization of synthesized *o*-Cu_2O NCs.

Sr no	Parameters	Results
1	BETsurface area (m^2g^{-1})	0.057
2	Average pore diameter (A°)	106.82
3	Adsorption average pore width (4 V A^{o-1} by BET)(A°)	707.84
4	Pore volume(cm^3g^{-1})	0.00
5	Total volume in pores(cm^3g^{-1})	0.00099(by DFT)
6	Total area in pores(m^2g^{-1})	0.141(by DFT)

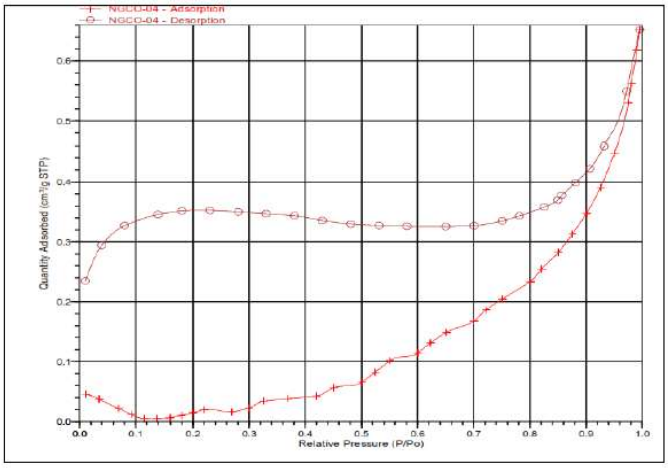

Fig. 2.19 Nitrogen adsorption- desorption isotherm of as-synthesized *o*-Cu_2O NCs.

Table 2.9 Scope of the substrates undergoing oxidation in presence of *o*-Cu_2O NCs and under optimized reaction parameters.

The carbonyl products obtained on oxidation of corresponding hydrocarbon having benzylic sp^3 C-H bond. The numbers indicate: Yield% (benzylic sp^3 C-H bond dissociation energy of the substrate in kcal/mol).	Compounds which could not undergo oxidation at the end of the 6th day. [a] Values in parenthesis indicate C-H BDE (next to functional group) in kcal/mol.
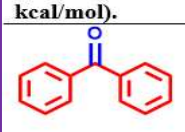 92% (84.5±0.5) 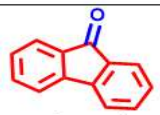 92% (82.0±2) 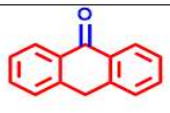 93% (76.3) 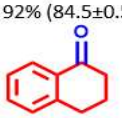 87% (82.6) 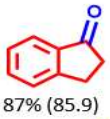 87% (85.9) 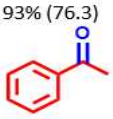 75% (85.4±1.5) 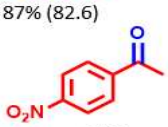 92% 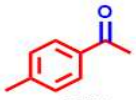 70% 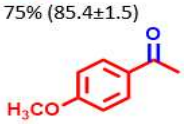 70% 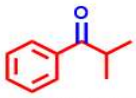 73% (89.7±1.2)	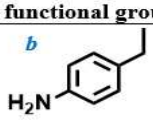 (97.0) 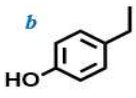  (95.0) 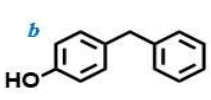 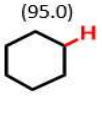 (96.2) 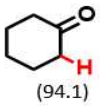 (94.1) 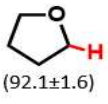 (92.1±1.6) 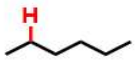 (98.0) 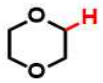 (96.0) 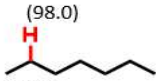 (98.0)
	[a]Color of NCs changes from red to green.[b]Expected oxidation product i.e. carbonyl compound is not formed.

2.7 Recovery and recycling of the catalyst. The *o*-Cu_2O NCs were recovered and recycled for three consecutive model reaction cycles under oxygen atmosphere. The catalytic activity was lost almost by 10% for each cycle without affecting the selectivity for the carbonyl product. The HRSEM analysis of catalyst, recovered at the end of each day up to six days, was carried out to study the change in its morphology (Fig. 2.20). It can be observed that the catalyst could preserve its shape and dispersity for up to six days with little agglomeration. However, on the fourth cycle, its activity becomes the same as bulk Cu_2O. We had also carried out the model reaction under a normal aerial atmosphere in the dark for six days and recovered the catalyst at the end of each day. It can be observed that the catalyst morphology was preserved for almost three days with little agglomeration, and it destroyed after four days (Fig. 2.21). PXRD of the recovered catalyst (at the end of the sixth day in dark) was carried out (Fig. 2.22). The major diffraction peaks at 2θ values at 29.68°, 36.07°, 42.86°, 62.05°, 73.97°, and 77.89° corresponding to the refraction from (110), (111), (200), (220), (311), and (222) planes,

respectively, confirming the original cuprite phase of Cu_2O NCs. The noise before 29^o is due to surface adsorbed organic impurities responsible for the slight deterioration in catalytic activity for the next cycle. This observation confirmed that the phase of the Cu_2O NCs does not affected when the organic transformation is carried out in the dark condition.

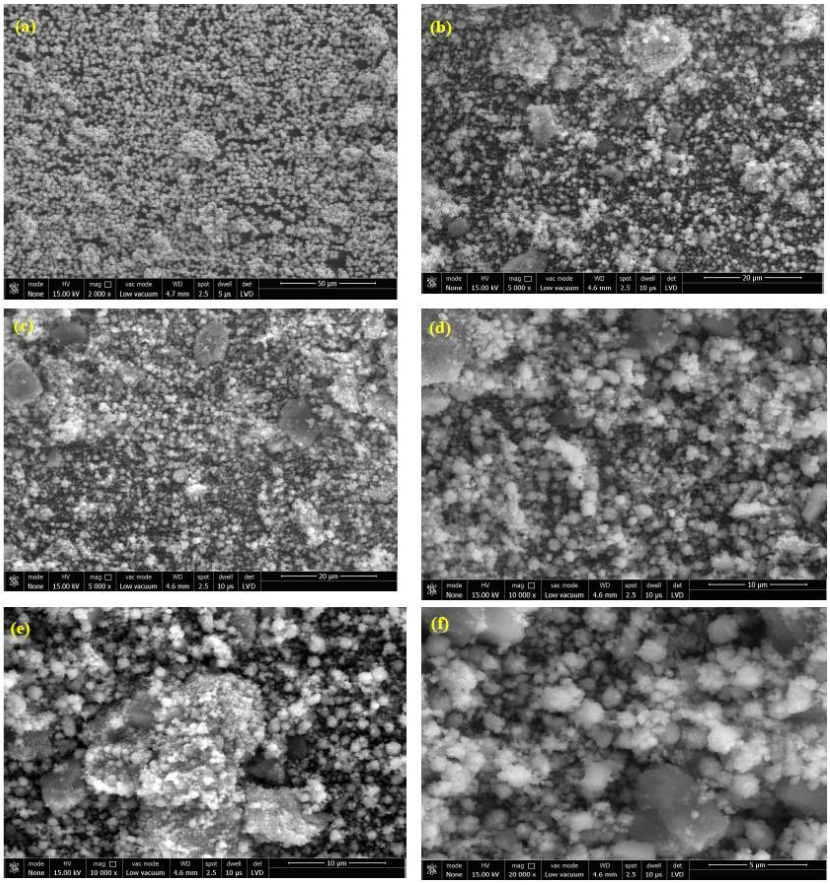

Fig. 2.20 HRSEM images of recovered *o*-Cu_2O when the model reaction was carried out under oxygen atmosphere, at the end of (a) day 1 (b) day 2 (c) day3 (d) day 4 (e) day 5 and (f) day 6.

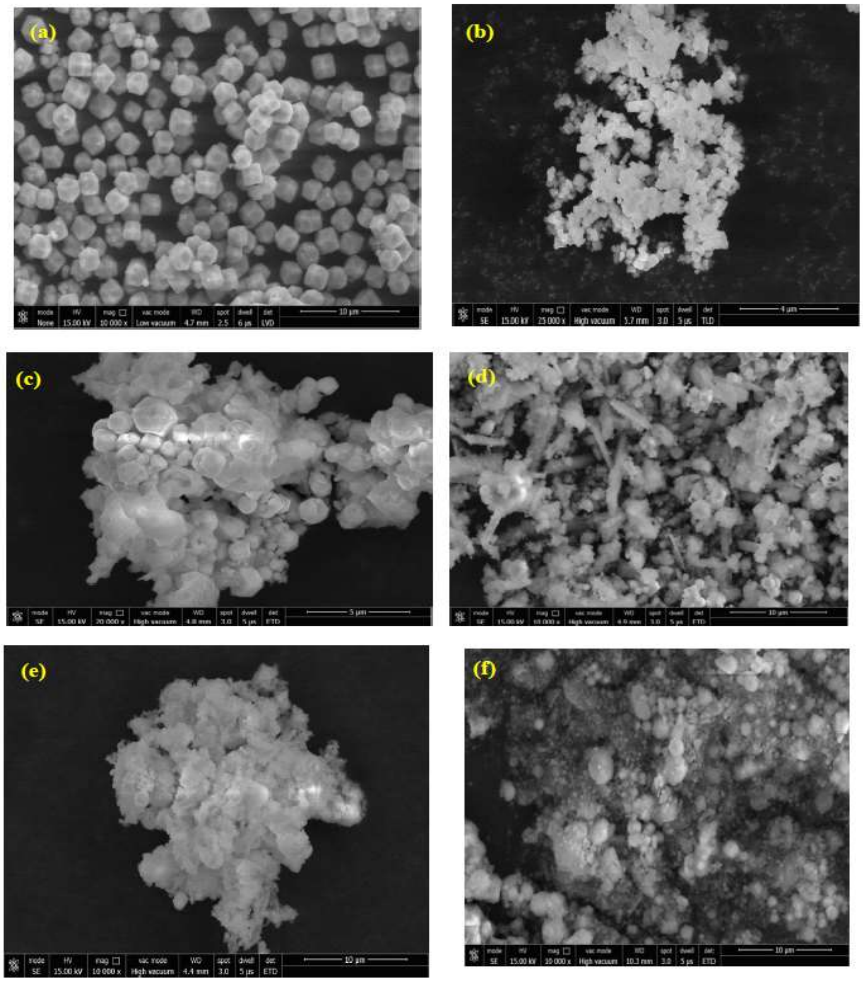

Fig. 2.21 HRSEM images of recovered *o*-Cu_2O when the model reaction was carried out in dark, at the end of (a) day 1 (b) day 2 (c) day3 (d) day 4 (e) day 5 and (f) day 6.

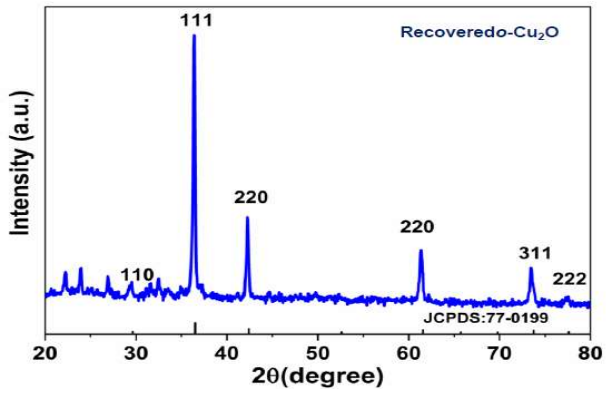

Fig. 2.22 Powder XRD of recovered *o*-Cu_2O at the end of sixth day when the model reaction was carried out in dark.

2.8 Conclusion

(111) faceted Cu_2O nanocrystals having octahedral morphology have been synthesized and characterized. The exposed (111) facets of Cu_2O NCs were explored as catalytic sites for the benzylic sp^3C-H bond oxidation process. From the optimization of oxidation of DPM as model reaction, free radical scavenger experiments and special experiments, following conclusions can be drawn: (1) Cu^{1+} ended (111) facets of *o*-Cu_2O NCs are capable to activate oxygen molecules to undergo reduction by SET mechanism in presence of light, and the in situ generated superoxo species immediately abstract the ·H radical from the nearby substrate and initiate the cascade of chemical reactions and electronic processes resulting into stable oxidation product and complete restructuring of the crystal lattice of the catalyst, respectively (2) The etching of the (111) surfaces during the oxidation process can be avoided if the reaction is carried out in dark or under inert atmosphere or under continuous flow of oxygen gas (3) The developed protocol for benzylic sp^3C-H bond oxidation to ketone is applicable under mild conditions with complete selectivity just by stirring the reaction mixture over bar magnet for 4 days (4) Also, this protocol is equally and effectively applicable to the wide range of substrates having C-H bond energy less than 90 kcal/mol (5) The (111) facets of *o*-Cu_2O NCs can be regenerated for the successive three catalytic cycles with minute loss in reactivity by maintaining the proper reaction conditions.

Exciting results were obtained for the oxidation of hetero benzylic sp^3 C-H bond on the (111) facets of the as-synthesized *o*-Cu_2O NCs which will be reported in a separate study. It would be interesting to study the fate of oxidation reactions on the other facets of lower Millar indices like (001), (101), (110) etc. of Cu_2O nanocrystals which will be the focus of our next study.

Oxidation of diphenylmethane (Reaction I). 0.166 mL diphenylmethane (1.0 mmol) was dissolved in 6.0 mL acetonitrile in 10.0 mL round bottom flask and stirred for 5 min. *o*-Cu_2O NCs (3.5 mol%) were subsequently added and the mixture was stirred for 10 min. Finally, 0.52 mL t-butyl hydroperoxide (TBHP, 4.0 mmol) was added, and the reaction mixture was stirred for 6 days at RT. The reaction progress was monitored on the TLC plate every 4 h (for optimization of reaction parameters). After completing the reaction (96 h), the reaction mixture was centrifuged to recover the catalyst; the excess of TBHP was destroyed by adding excess sodium metabisulphite into the reaction mixture. The excess reagents were distilled out. The product was extracted with ethyl acetate and dried over sodium sulphate. The crude product was purified by column chromatography using petroleum ether (60-80°C) as eluent. The

product obtained was analysed by ^{1}H-NMR. The same reaction protocol was followed for all the substrates and reactions discussed.

Diphenylmethanone. White crystal; m.p. 47-49°c. ^{1}H-NMR ($CDCl_3$, 400 MHz,): δ 7.84-7.81 (m, 4H,), 7.61-7.59 (m, 2H,), 7.52-7.28 (m, 4H). (Fig. 2.23)^{13}C NMR ($CDCl_3$, 100 MHz) δ (ppm): 194.8, 137.5, 132.4, 130.1, 128.3. Purified by column chromatography on silica gel- 10% EtOAc in petroleum ether as a mobile phase. (Fig. 2.24)

1-Phenylethanone. Colorless viscous liquid; ^{1}H NMR ($CDCl_3$, 400 MHz): δ 7.90- 7.86 (m, 2H), 7.51-7.46 (m, 1H), 7.41-7.36 (m, 2H), 2.53-2.51 (s, 3H). (Fig. 2.25)^{13}C NMR ($CDCl_3$, 100 MHz) δ (ppm): 198.2, 137.1, 133.1, 128.3, 26.6. Purified by column chromatography on silica gel- 10% EtOAc in petroleum ether as a mobile phase. (Fig. 2.26)

2-Methyl-1-phenyl-1-propanone. Colorless liquid; b.p 217 °C. ^{1}H NMR ($CDCl_3$, 400 MHz) δ (ppm): 7.95 (d, J = 7.6 Hz, 2H), 7.55 (t, J = 7.6 Hz, 1H), 7.46 (t, J = 7.6 Hz, 2H), 3.57-3.56 (m, 1H), 1.25-1.14 (d, J = 7.2 Hz, 6H); (Fig. 2.27)^{13}C NMR ($CDCl_3$, 100 MHz) δ (ppm): 204.6, 136.2, 132.8, 128.6, 128.3, 35.4, 19.2. Purified by column chromatography on silica gel- 10% EtOAc in petroleum ether as a mobile phase. (Fig. 2.28)

2,3-Dihydro-1H-inden-1-one (1-indanone). White solid; m.p. = 39-41 °C, ^{1}H-NMR ($CDCl_3$, 400 MHz): δ (ppm): 7.76 (d, J = 7.6 Hz, 1H), 7.58 (t, J = 7.6 Hz, 1H), 7.48 (d, J = 7.6 Hz, 1H), 7.37 (t, J = 7.6 Hz, 1H), 3.14 (t, J = 6.0 Hz, 2H), 2.69 (t, J = 6.0 Hz, 2H); (Fig. 2.29)^{13}C NMR ($CDCl_3$, 100 MHz) δ (ppm): 207.2,155.2, 137.1, 134.4, 127.3, 126.7, 123.7, 36.2, 29.7, 25.8. Purified by column chromatography on silica gel- 10% EtOAc in petroleum ether as a mobile phase. (Fig. 2.30)

3,4-Dihydro-2H-napthalen-1-one (1-Tetralone). Clear amber to brown oily liquid; m.p. = 2-7 °C. ^{1}H-NMR ($CDCl_3$,400 MHz): δ 8.02 (d, J = 8 Hz, 1H), 7.46 (t, J = 7.4 Hz, 1H), 7.32-7.23 (m, 2H), 2.96 (t, J = 6 Hz, 2H), 2.65 (t, J = 6.5 Hz, 2H), 2.18-2.08 (m, 2H). (Fig. 2.31)^{13}C NMR ($CDCl_3$, 100 MHz) δ (ppm): 198.5, 144.5, 133.4, 132.6, 128.8, 127.2, 126.7, 39.2, 29.7, 23.3. Purified by column chromatography on silica gel- 10% EtOAc in petroleum ether as a mobile phase. (Fig. 2.32)

9H-fluorene-9-one (Fluorenone). Pale yellow solid; m.p. = 84-85 °C. ^{1}H NMR ($CDCl_3$, 400 MHz) δ (ppm): 7.66 (d, J = 7.5 Hz, 2H), 7.55-7.50 (m, 4H), 7.33-7.25 (m, 2H); (Fig. 2.33)^{13}C NMR ($CDCl_3$, 100 MHz) δ (ppm): 194.0, 144.4, 133.7, 134.2, 129.1, 124.3, 120.3. Purified by column chromatography on silica gel- 10% EtOAc in hexane as a mobile phase. (Fig. 2.34)

9, 10-dioxoanthracene (Anthraquinone). Yellow Solid; m.p. = 286 °C, ^{1}H NMR ($CDCl_3$, 400 MHz) δ (ppm): 7.85-7.81 (d, J = 3.2, 4H), 8.35-8.33 (dd, J = 3.6, 4H). (Fig. 2.35)^{13}C NMR ($CDCl_3$, 100 MHz) δ (ppm): 183.2, 134.1, 133.5, 123.2. Purified by column chromatography on silica gel- 10% EtOAc in hexane as a mobile phase. (Fig. 2.36)

1-(4-Nitrophenyl) ethanone. Slightly yellowish crystalline powder; m.p. = 103 to 106 °C,. ^{1}H NMR ($CDCl_3$, 400MHz) δ (ppm): 8.15-8.12 (d, J = 8.8, 2H), 8.35-8.33 (d, J = 9.2, 2H), 2.71(s, 3H). Purified by column chromatography on silica gel- 10% EtOAc in hexane as a mobile phase. (Fig. 2.37)

1-(4-Methoxyphenyl) ethanone. White solid; m.p. = 39-40 °C, ^{1}H NMR ($CDCl_3$, 400 MHz) δ (ppm): 7.93 (d, J = 8.8 Hz, 2H), 6.93 (d, J = 8.8 Hz, 2H), 3.88 (s, 3H), 2.57 (s, 3H). Purified by column chromatography on silica gel- 10% EtOAc in hexane as a mobile phase. (Fig. 2.38)

1-(4-Methylphenyl) ethanone. Colorless liquid, b.p = 226 °C. ^{1}H NMR ($CDCl_3$, 400 MHz) δ (ppm): 7.88-7.86 (d, J = 8.0 Hz, 2H), 7.28-7.26 (d, J = 8.0 Hz, 2H), 2.59 (s, 3H), 2.42 (s, 3H). Purified by column chromatography on silica gel - 10% EtOAc in hexane as a mobile phase. (Fig. 2.39)

(4-(tert-butylperoxy) phenyl)(phenyl)methane. Slight yellowish liquid, ^{1}H NMR ($CDCl_3$, 400MHz) δ(ppm): 7.33-7.30 (m, 2H), 7.29-7.26 (t, J = 1.2 Hz, 1H), 7.24-7.22 (d, J = 8Hz, 2H), 7.06-7.04(d, J = 8 Hz, 2H), 6.89-6.22 (d, J = 3.2 Hz, 2H), 3.92 (s, 2H), 1.20 (s, 9H). (Fig. 2.40)

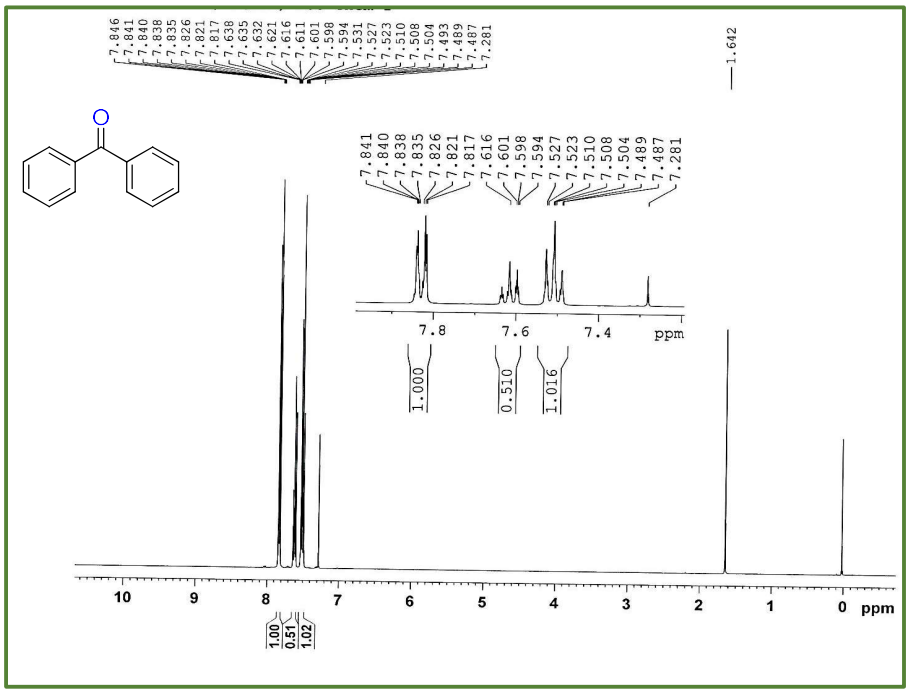

Fig. 2.23 ^{1}H NMR Diphenylmethanone(Benzophenone).

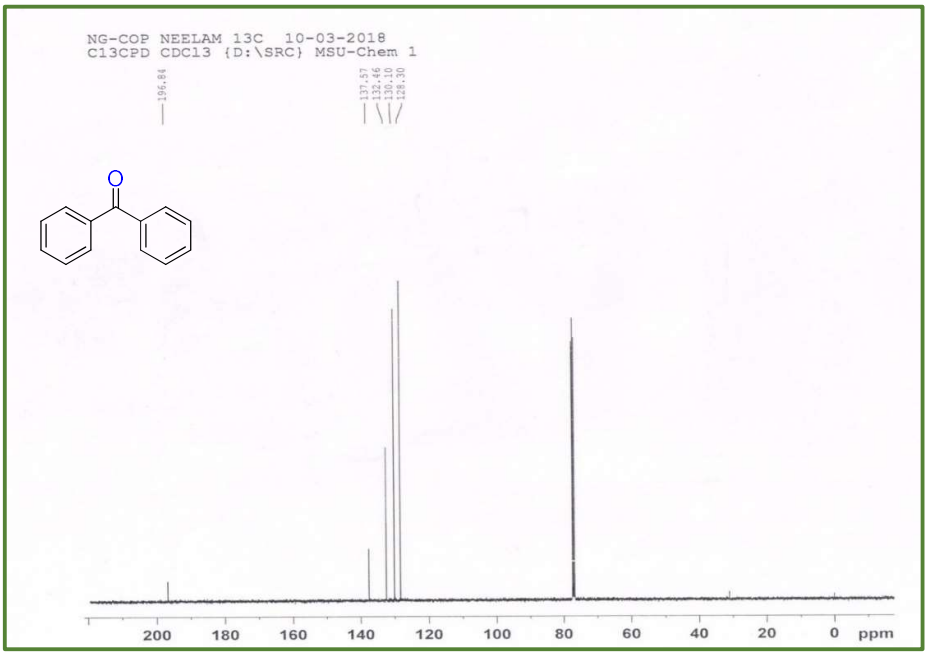

Fig. 2.24 ^{13}C NMR Diphenylmethanone (Benzophenone).

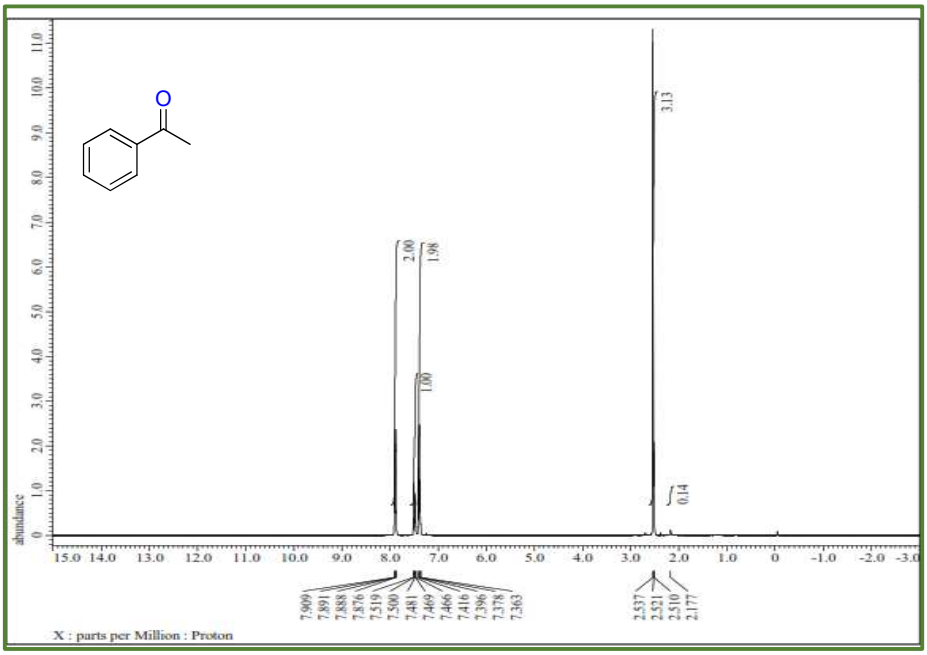

Fig. 2.25 ^{1}H NMR 1-Phenylethanone(Acetophenone).

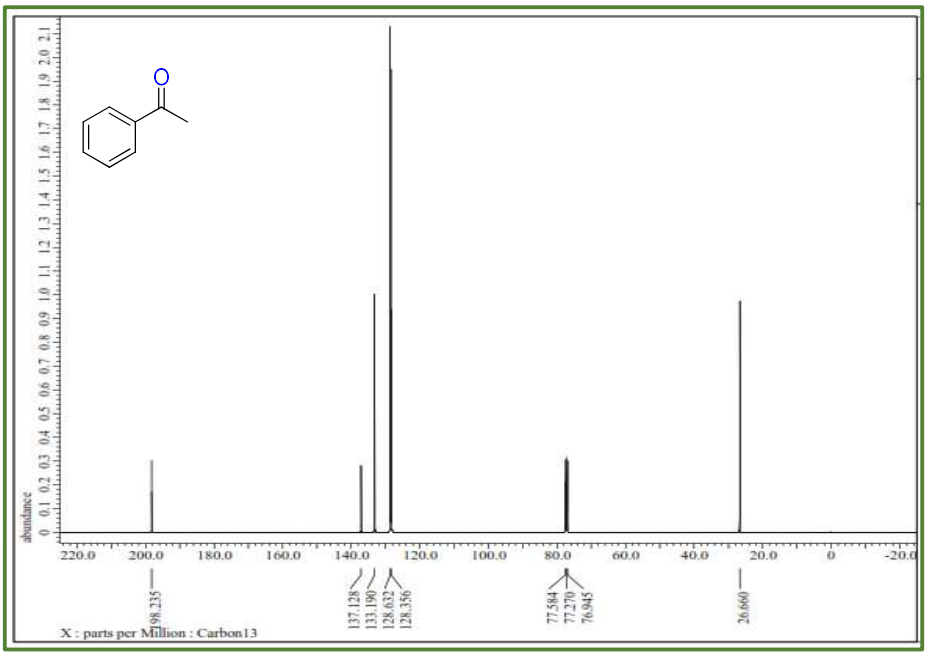

Fig. 2.26 ^{13}C NMR of 1-Phenylethanone(Acetophenone).

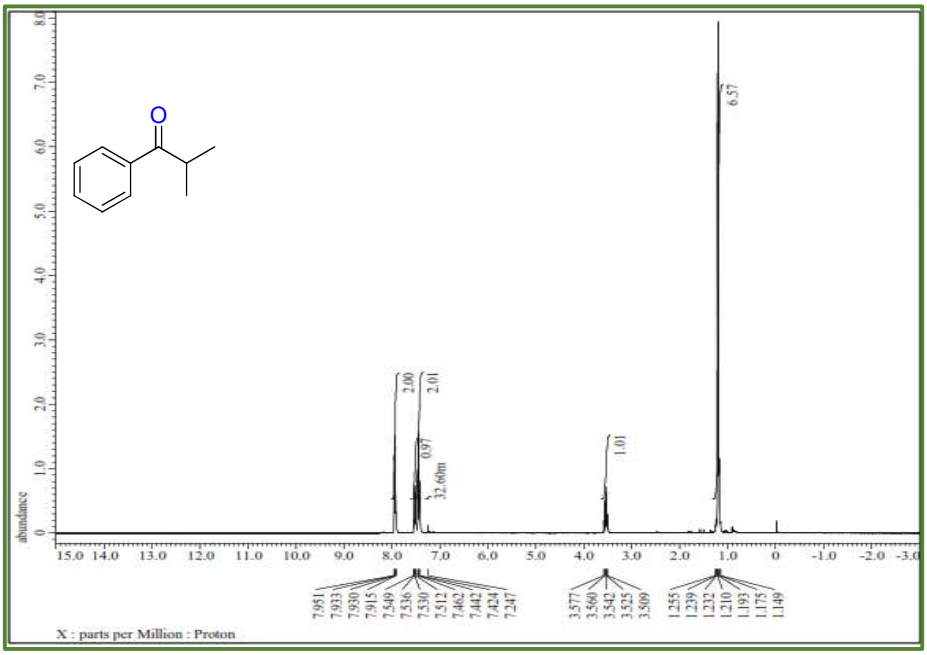

Fig. 2.27 ^{1}H NMR of 2-methyl-1-phenylpropane-1-one.

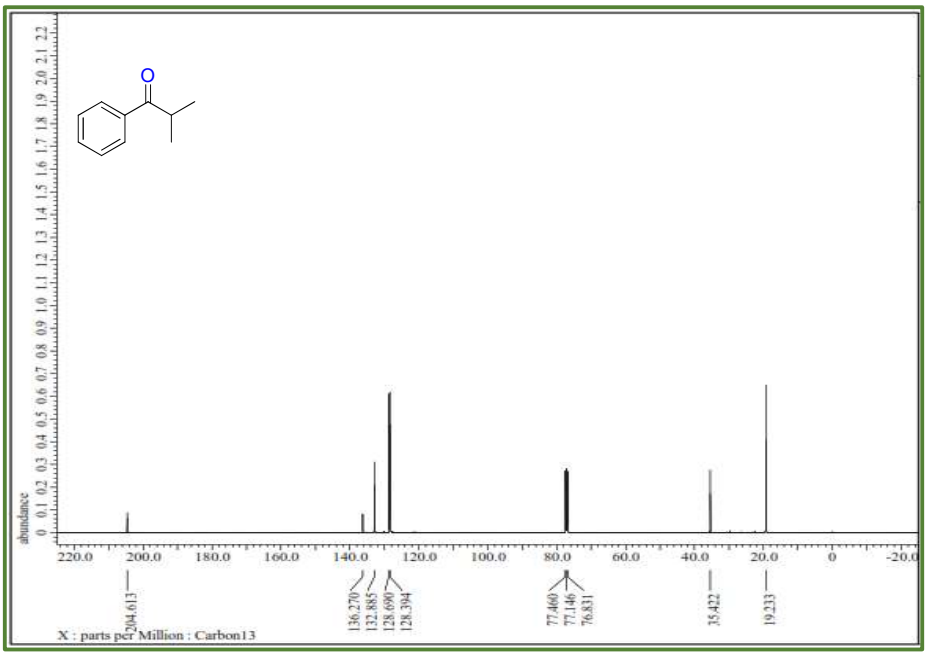

Fig. 2.28 ^{13} C NMR of 2-methyl-1-phenylpropane-1-one.

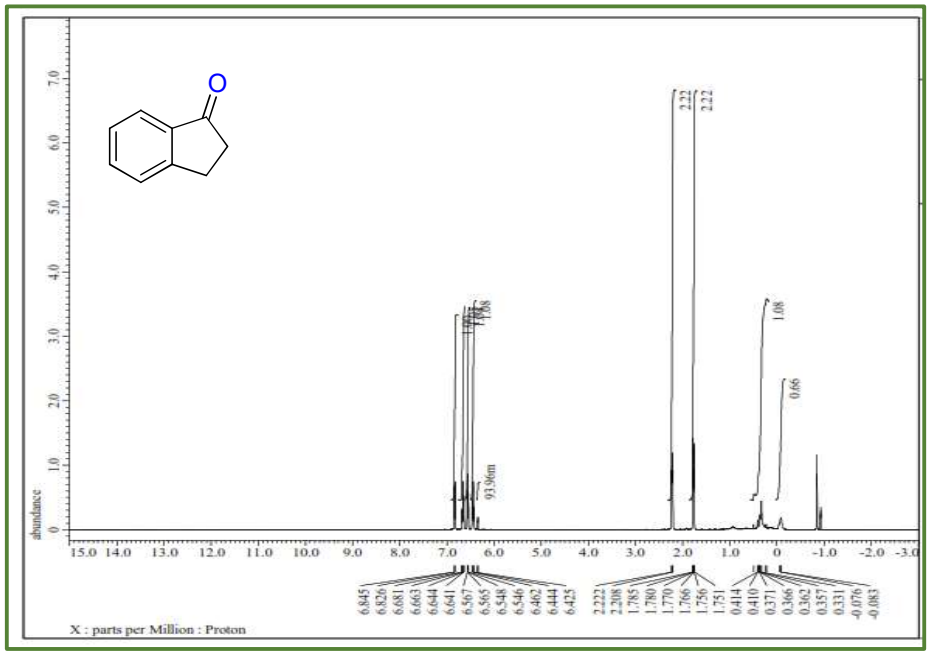

Fig. 2.29 ^{1}H NMR of 2,3-Dihydro-1H-inden-1-one(1-Indanone).

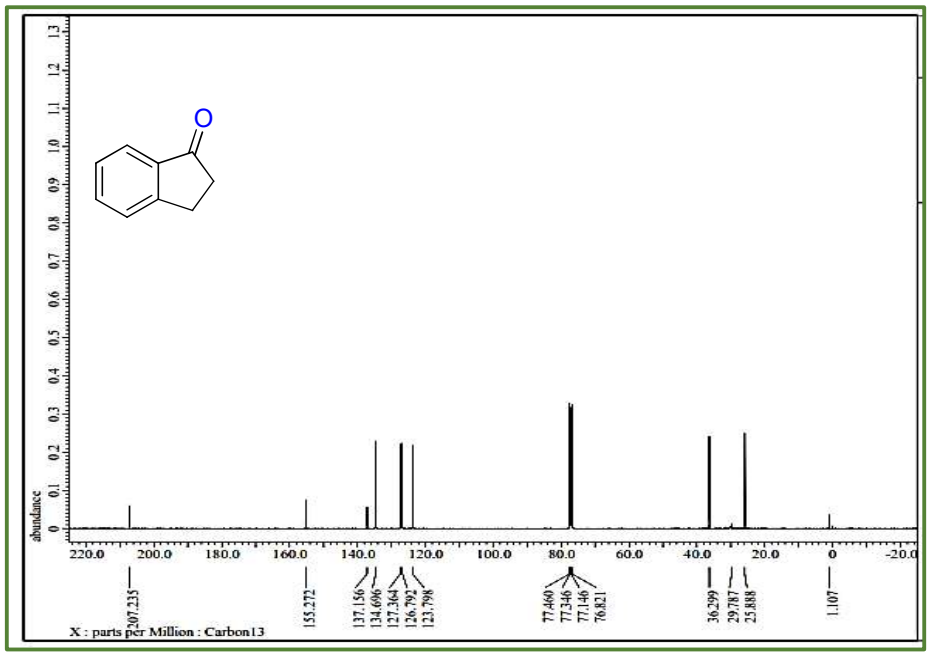

Fig. 2.30 ^{13} C NMR of 2,3-Dihydro-1H-inden-1-one(1-Indanone).

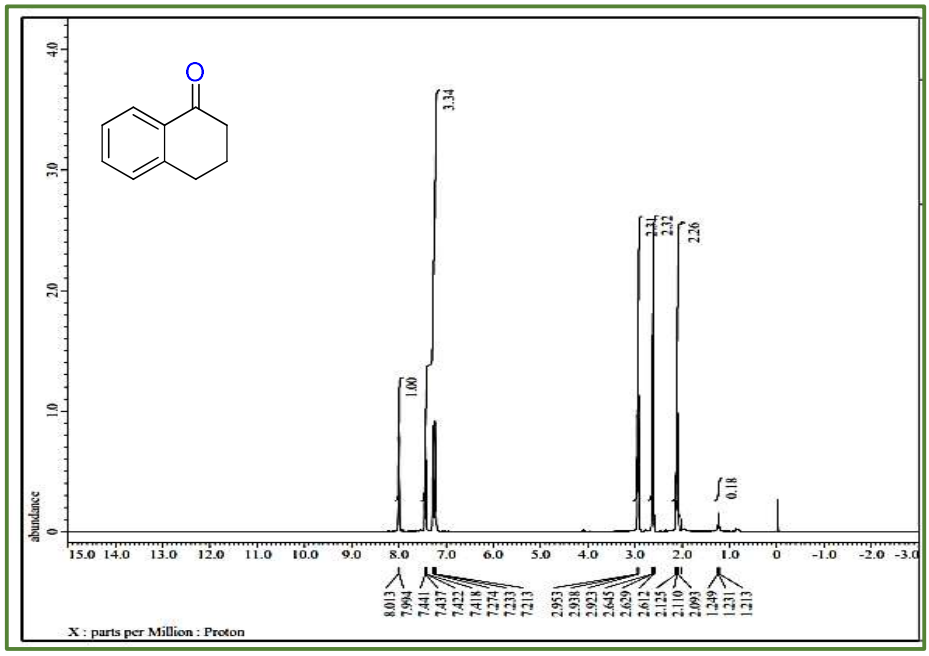

Fig. 2.31 ^{1}H NMR of 3,4-Dihydro-2H-napthalen-1-one(1-Tetralone).

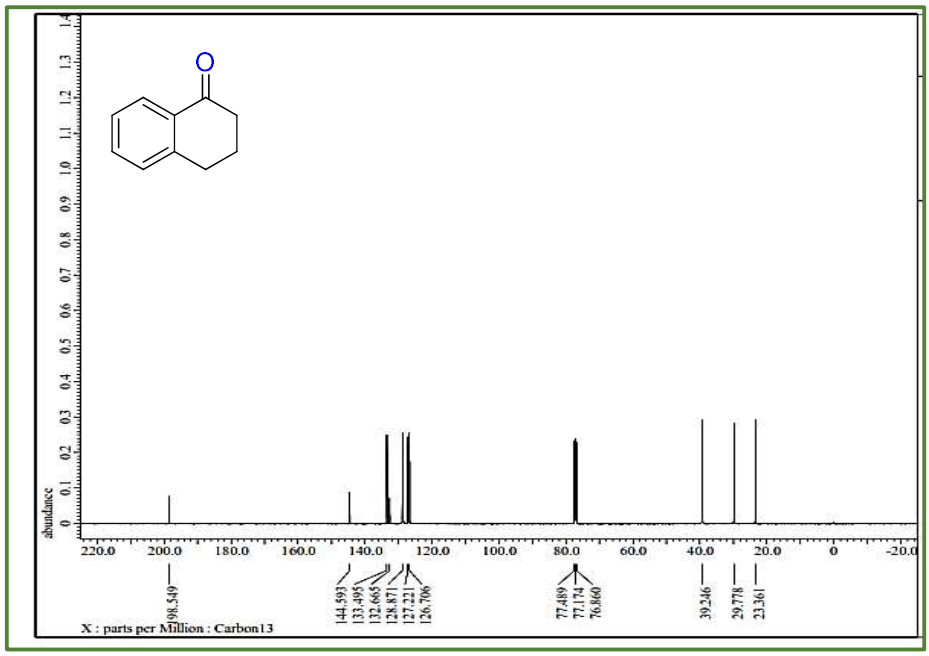

Fig. 2.32 ^{13}C NMR of 3,4-Dihydro-2H-napthalen-1-one (1-Tetralone).

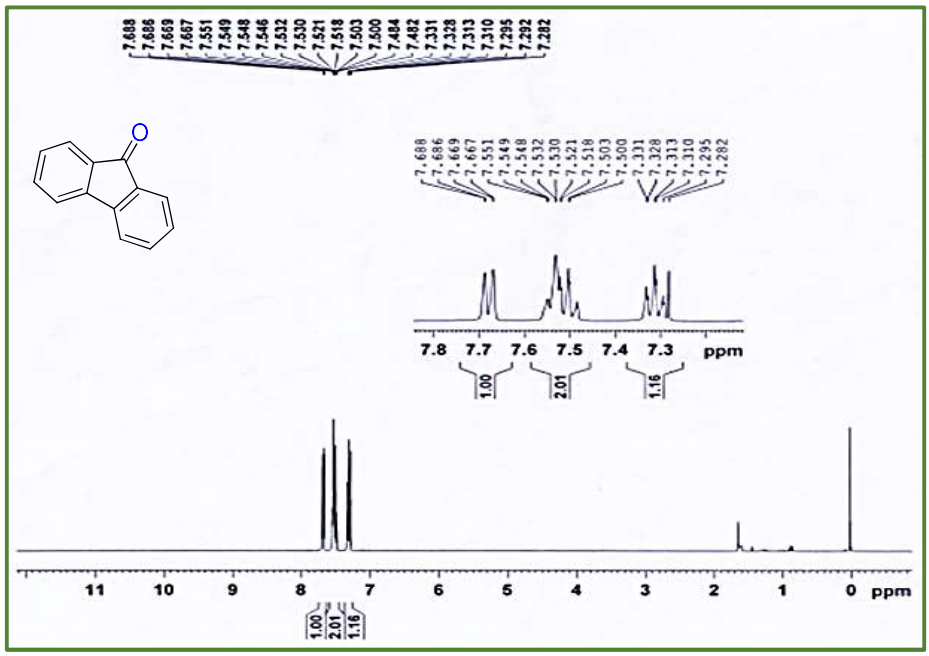

Fig. 2.33 ^{1}H NMR of 9H-fluorene-9-one (Fluorenone).

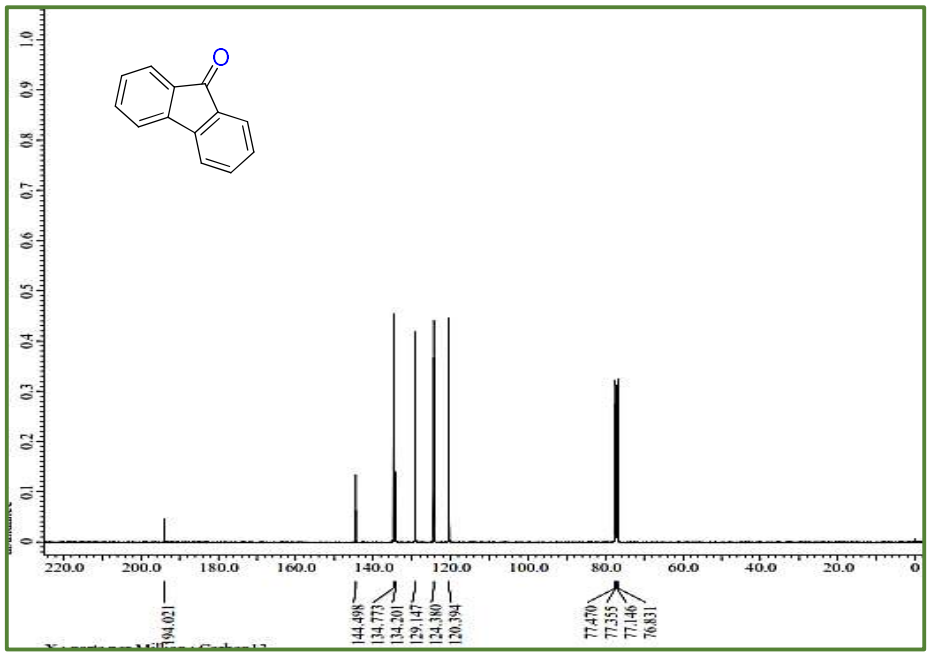

Fig. 2.34 ^{13}C NMR of 9H-fluorene-9-one (Fluorenone).

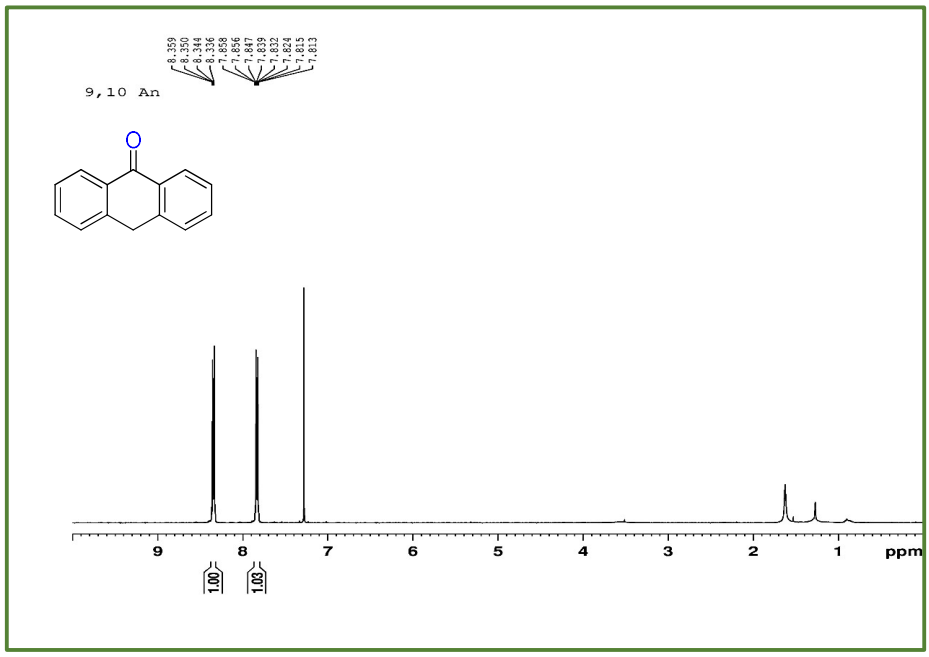

Fig. 2.35 ^{1}HNMR of 9,10-dioxoanthracene.

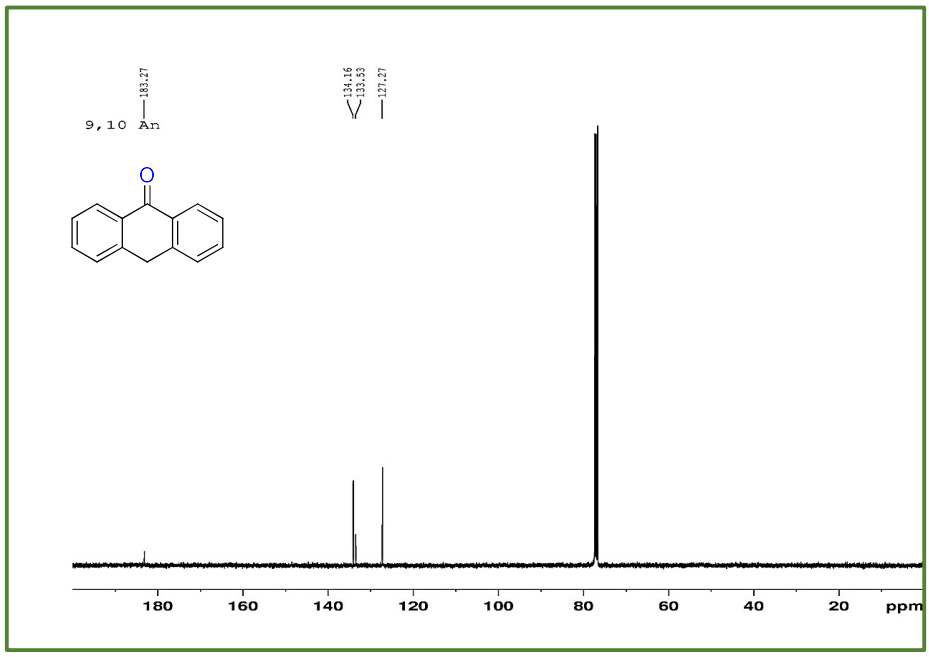

Fig. 2.36 ^{13}C NMR of 9,10-dioxoanthracene.

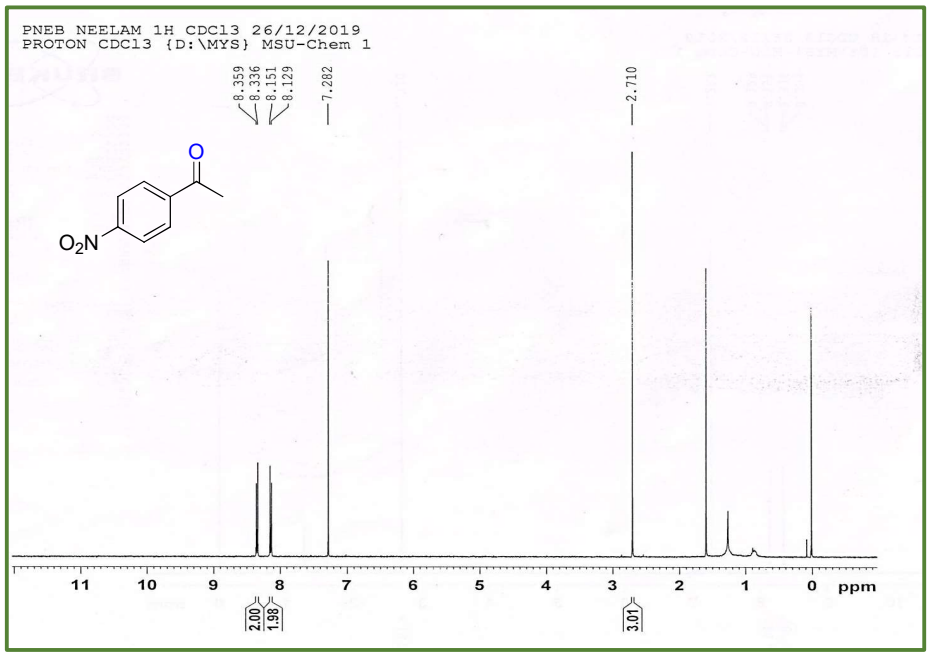

Fig. 2.37 ^{1}H NMR of 4-Nitroacetophenone.

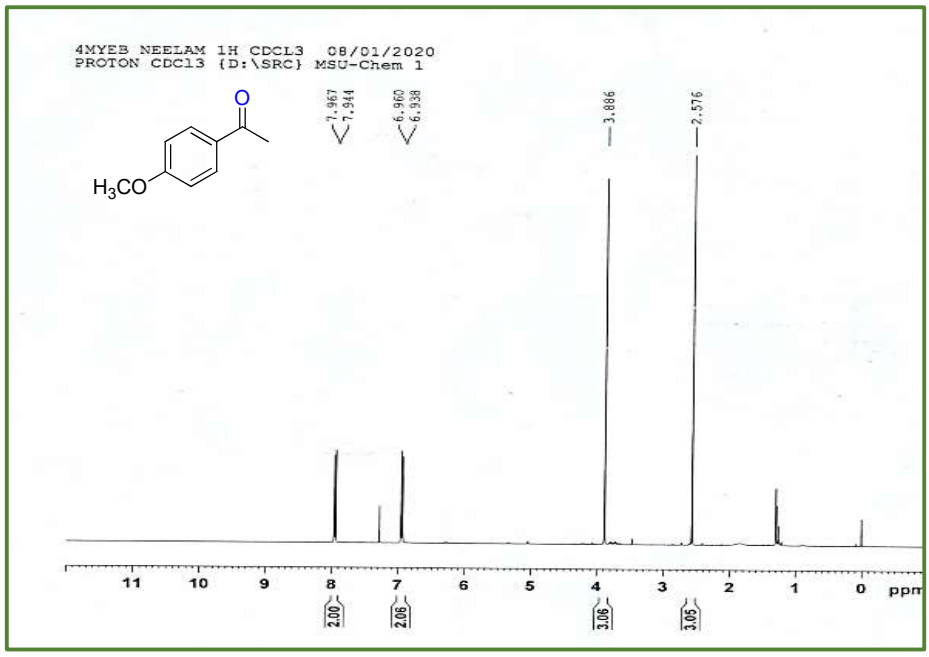

Fig. 2.38 ^{1}H NMR of 4-Methoxyacetophenone.

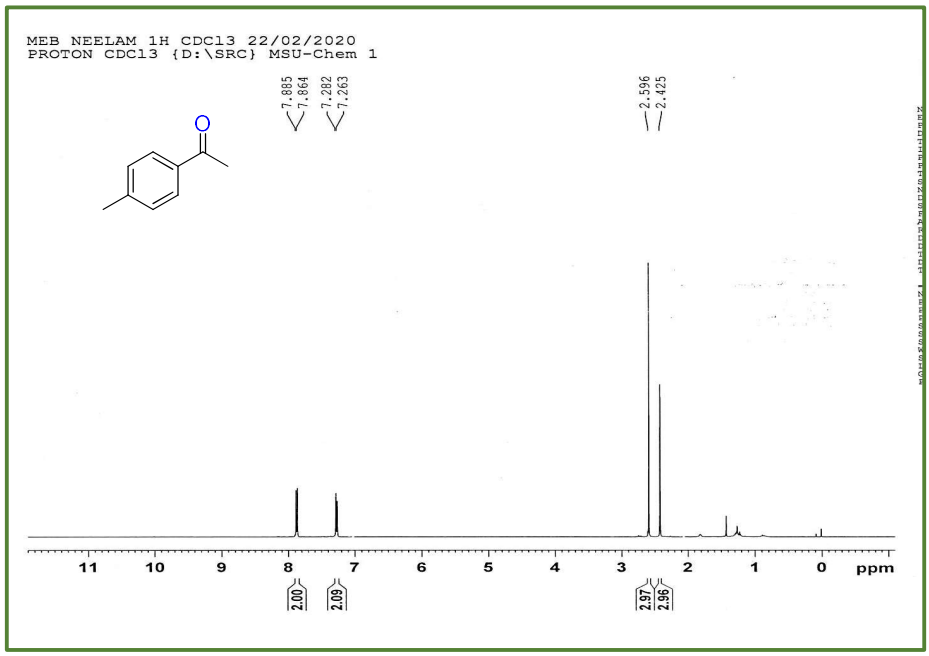

Fig. 2.39 ^{1}H NMR of 4-Methylacetophenone.

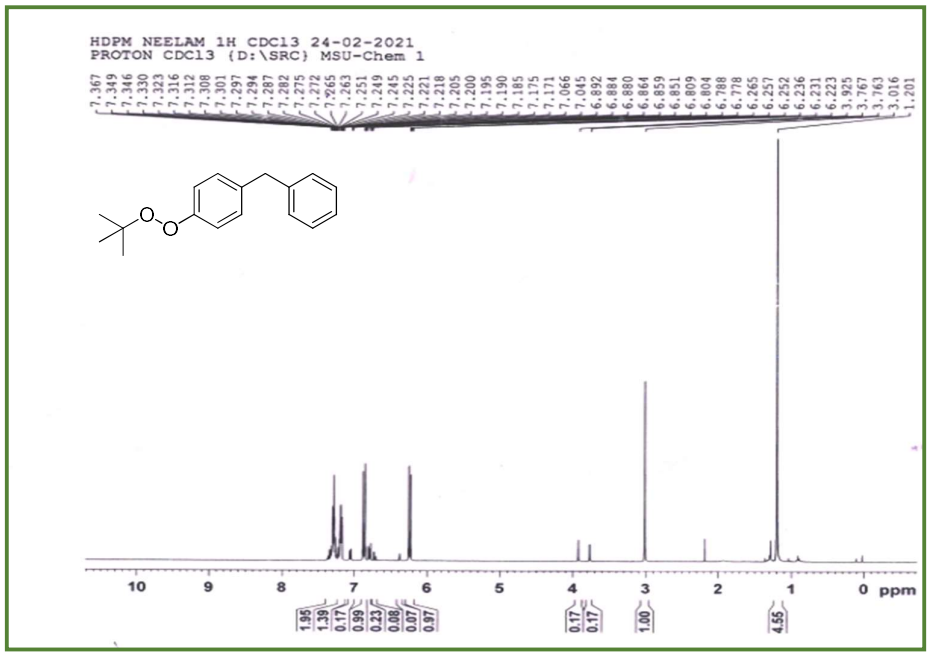

Fig. 2.40 ^{1}H NMR of (4-(tert-butylperoxy) phenyl)(phenyl)methane. NMR spectra of 6th day reaction mixture was recorded directly showing presence of unreacted reactant in minute quantity.

2.9 References

(1) Yun, L.; Zhao, J.; Tang, X.; Ma, C.; Yu, Z.; Meng, Q. Selective Oxidation of Benzylic Sp^3C-H Bonds Using Molecular Oxygen in a Continuous-Flow Microreactor. *Org. Process Res. Dev.* **2021**, 25, 1612–1618.

(2) A. Arndtsen, B.; G. Bergman, R.; Andrew Mobley, T.; H. Peterson, T. Selective Intermolecular Carbon-Hydrogen Bond Activation by Synthetic Metal Complexes in Homogeneous Solution. *Acc. Chem. Res.* **2002**, *28*, 154–162.

(3) Sharma, A. S.; Kaur, H. Sustainable Protocol for Benzylic -CH_2 Oxidation with Dioxygen to Phenones Using AuNPs@ Resin Beads. *ChemistrySelect* **2017**, *2*, 10112–10117.

(4) Jones, W. D. The Effects of Ancillary Ligands on Metal–Carbon Bond Strengths as Determined by C–H Activation. *Top Organomet Chem* **2016**, *56*, 67–90.

(5) Wang, Y.; Wang, Y.; Kuang, Y. Rh2(Esp)2-Catalyzed Allylic and Benzylic Oxidations. *Chem. Commun.* **2015**, 51, 5852–5855.

(6) Zhang, J.; Wang, Z.; Wang, Y.; Wan, C.; Zheng, X.; Wang, Z. A Metal-Free Catalytic System for the Oxidation of Benzylic Methylenes and Primary Amines under Solvent-Free Conditions. *Green Chem.* **2009**, *11*, 1973–1978.

(7) Hruszkewycz, D. P.; Miles, K. C.; Thiel, O. R.; Stahl, S. S. Co/NHPI-Mediated Aerobic Oxygenation of Benzylic C-H Bonds in Pharmaceutically Relevant Molecules. *Chemi. Sci.* **2017**, *8*, 1282–1287.

(8) Yi, H.; Bian, C.; Hu, X.; Niu, L.; Lei, A. Visible Light Mediated Efficient Oxidative Benzylic Sp^3 C-H to Ketone Derivatives Obtained under Mild Conditions Using O_2. *Chem.l Commun.* **2015**, *51*, 14046–14049.

(9) Bai, Y.; Yang, T.; Gu, Q.; Cheng, G.; Zheng, R. Shape Control Mechanism of Cuprous Oxide Nanoparticles in Aqueous Colloidal Solutions. *Powder Technol.* **2012**, *227*, 35–42.

(10) K. Machhi, H.; K. Sonigara, K.; N. Bariya, S.; P. Soni, H.; S. Soni, S. Hierarchically Porous Metal–Organic Gel Hosting Catholyte for Limiting Iodine Diffusion and Self-Discharge Control in Sustainable Aqueous Zinc–I_2 Batteries. *ACS Appl. Mater. Interfaces* **2021**, *13*, 21426–21435.

(11) P. Giannozzia, O. Andreussib,i, T. Brummec, O. Bunaud, M. Buongiorno Nardellie, M. Calandrad, R. Carf, C. Cavazzonig, D. Ceresolih, M. C. et al. Advanced Capabilities for Materials Modelling with Quantum ESPRESSO. *Mater. Res. Express* **2019**, 0–12.

(12) Stefan Grimme, Stephan Ehrlich, L. G. Effect of the Damping Function in Dispersion Corrected Density Functional Theory . *J. Comput. Chem*. **2012**, *32*, 174–182.

(13) Hendrik J. Monkhorst and James D. Pack. Special Points for Brillonin-Zone Integrations. *Paper Knowledge . Toward a Media History of Documents* **2014**, *13*, 5188–5192.

(14) Pal, J.; Ganguly, M.; Mondal, C.; Roy, A.; Negishi, Y.; Pal, T. Crystal-Plane-Dependent Etching of Cuprous Oxide Nanoparticles of Varied Shapes and Their Application in Visible Light Photocatalysis. *J. Phys. Chem. C* **2013**, *117*, 24640–24653.

(15) Snyder, R. J. and R. L. Introduction to X-ray powder diffractometry. *John Wiley and Sons, New York 1996* **2011**, *11*, 277–278.

(16) Zhang, D. F.; Zhang, H.; Guo, L.; Zheng, K.; Han, X. D.; Zhang, Z. Delicate Control of Crystallographic Facet-Oriented Cu_2O Nanocrystals and the Correlated Adsorption Ability. *J. Mater. Chem* **2009**, *19*, 5220–5225.

(17) Berg, J. M.; Romoser, A.; Banerjee, N.; Zebda, R.; Sayes, C. M. The Relationship between PH and Zeta Potential of ∼ 30 Nm Metal Oxide Nanoparticle Suspensions Relevant to in Vitro Toxicological Evaluations. *Nanotoxicology* **2009**, *3*, 276–283.

(18) Tan, J.; Zheng, T.; Yu, Y.; Xu, K. TBHP-Promoted Direct Oxidation Reaction of Benzylic Csp^3-H Bonds to Ketones. *RSC Adv.* **2017**, *7*, 15176–15180.

(19) Wang, H.; Wang, Z.; Huang, H.; Tan, J.; Xu, K. KOtBu-Promoted Oxidation of (Hetero)Benzylic Csp^3-H to Ketones with Molecular Oxygen. *Org. Lett.* **2016**, *18*, 5680–5683.

(20) Yin, M.; Wu, C.-K.; Lou, Y.; Burda, C.; T. Koberstein, J.; Zhu, Y.; O'Brien, S. Copper Oxide Nanocrystals. *J. Am. Chem.l Soc.* **2005**, *127*, 9506–9511.

(21) Robert, T.; Bartel, M.; Offergeld, G. Characterization of Oxygen Species Adsorbed on Copper and Nickel Oxides by X-Ray Photoelectron Spectroscopy. *Surf. Sci.* **1972**, *33*, 123–130.

(22) B. Demissie, T.; H. Hansen, J. Mechanism and Site Selectivity in Visible-Light Photocatalyzed C–H Functionalization: Insights from DFT Calculations. *J. Org. Chem.* **2016**, *81*, 7110–7120.

(23) Chu, C. Y.; Huang, M. H. Facet-Dependent Photocatalytic Properties of Cu_2O Crystals Probed by Using Electron, Hole and Radical Scavengers. *J. Mater. Chem. A* **2017**, *5*, 15116–15123.

(24) T. Sawyer, D.; S. Valentine, J. How Super Is Superoxide? Acc. Chem. Res. **2002**, *14*, 393–400.

(25) H. Huang, M.; Naresh, G.; Chen, H.-S. Facet-Dependent Electrical, Photocatalytic, and Optical Properties of Semiconductor Crystals and Their Implications for Applications. *ACS Appl. Mater. Interfaces* **2017**, *10*, 4–15.

(26) R. Hoffmann, M.; T. Martin, S.; Choi, W.; W. Bahnemann, D. Environmental Applications of Semiconductor Photocatalysis. *Chem. Rev.* **2002**, *95*, 69–96.

(27) Sun, Y.; J. Pignatello, J. Evidence for a Surface Dual Hole-Radical Mechanism in the Titanium Dioxide Photocatalytic Oxidation of 2,4-D. *Environ. Sci. Technol* **2002**, *29*, 2065–2072.

(28) T. Martin, S.; T. Lee, A.; R. Hoffmann, M. Chemical Mechanism of Inorganic Oxidants in the TiO2/UV Process: Increased Rates of Degradation of Chlorinated Hydrocarbons. *Environ. Sci. Technol.* **2002**, *29*, 2567–2573.

(29) Spodine, E.; Manzur, J. Oxygen Insertion in Organic Substrates Catalyzed by Copper Compounds. *Coord. Chem. Rev.* **1992**, *119*, 171–198.

(30) J. Cramer, C.; B. Tolman, W. Mononuclear $Cu–O_2$ Complexes: Geometries, Spectroscopic Properties, Electronic Structures, and Reactivity. *Acc. Chem. Res.* **2007**, *40*, 601–608.

(31) Trammell, R.; Rajabimoghadam, K.; Garcia-Bosch, I. Copper-Promoted Functionalization of Organic Molecules: From Biologically Relevant Cu/O_2 Model Systems to Organometallic Transformations. *Chem. Rev.* **2019**, *119*, 2954–3031.

(32) Tano, T.; Okubo, Y.; Kunishita, A.; Kubo, M.; Sugimoto, H.; Fujieda, N.; Ogura, T.; Itoh, S. Redox Properties of a Mononuclear Copper(II)-Superoxide Complex. *Inorg. Chem* **2013**, *52*, 10431–10437.

(33) Chen, T.-N.; Kao, J.-C.; Zhong, X.-Y.; Chan, S.-J.; S. Patra, A.; Lo, Y.-C.; H. Huang, M. Facet-Specific Photocatalytic Activity Enhancement of Cu_2O Polyhedra Functionalized with 4-Ethynylanaline Resulting from Band Structure Tuning. *ACS Cent. Sci.* **2020**, *6*, 984–994.

(34) Shah, E.; Vaghasiya, J. V.; Soni, S. S.; Panchal, C. J.; Suryavanshi, P. S.; Chavda, M.; Soni, H. P. Ni Doped ZnS Nanoparticles as Photocatalyst: Can Mixed Phase Be Optimized for Better Performance? *J. Environ. Chem. Eng.* **2016**, *4*, 4708–4718.

(35) Niveditha, C. V.; Fatima, M. J. J.; Sindhu, S. Comprehensive Interfacial Study of Potentio-Dynamically Synthesized Copper Oxide Thin Films for Photoelectrochemical Applications. *J. Electrochem. Soc.* **2016**, *163*,

(36) Li, L.; Zhang, R.; Vinson, J.; L. Shirley, E.; P. Greeley, J.; R. Guest, J.; K. Y. Chan, M. Imaging Catalytic Activation of CO_2 on Cu_2O (110): A First-Principles Study. *Chemistry of Materials* **2018**, *30*, 1912–1923.

(37) Himes, R. A.; Karlin, K. D. Copper–Dioxygen Complex Mediated C–H Bond Oxygenation: Relevance for Particulate Methane Monooxygenase (PMMO). *Curr Opin Chem Biol* **2009**, *13*, 119–131.

(38) Ciano, L.; Davies, G. J.; Tolman, W. B.; Walton, P. H. Bracing Copper for the Catalytic Oxidation of C–H Bonds. *Nat. Catal* **2018**, *1*, 571–577.

(39) Newhouse, T.; Baran, P. S. If C-H Bonds Could Talk: Selective C-H Bond Oxidation. *Angew. Chem. Int. Ed.* **2011**, *50*, 3362–3374.

(40) Luo, Y.-R. *Handbook of Dissociation Energies in Organic Compounds By Yu-Ran Luo (University of South Florida, St. Petersburg). CRC Press LLC: Boca Raton. 2003.*

(41) Zhou, K.; Wang, X.; Sun, X.; Peng, Q.; Li, Y. Enhanced Catalytic Activity of Ceria Nanorods from Well-Defined Reactive Crystal Planes. *J. Catal.* **2005**, *229*, 206–212.

This work has been published in ACS Applied Nano Materials

https://pubs.acs.org/doi/10.1021/acsanm.1c01169

ACS APPLIED NANO MATERIALS

www.acsanm.org Article

Benzylic C_{sp^3}–H Bond Oxidation on the (111) Facets of Octahedral Cu_2O Nanocrystals

Neelam Gupta, Hiren K. Machhi, Bhumi A. Baraiya, Saurabh S. Soni, Ashutosh V. Bedekar, Prafulla K. Jha, and Hemant P. Soni*

Cite This: https://doi.org/10.1021/acsanm.1c01169 Read Online

ABSTRACT: Octahedral-shaped Cu_2O nanocrystals (o-Cu_2O NCs) have been synthesized by the wet chemical method. By powder X-ray diffraction (PXRD), X-ray photoelectron spectroscopy (XPS), field emission scanning electron microscopy (FESEM), and high-resolution transmission electron microscopy (HRTEM), it was confirmed that the synthesized material was Cu_2O NCs with octahedral morphology with the (111) facets exposed. The synthesized o-Cu_2O NCs have been explored as the catalyst for benzylic sp^3 C–H bond oxidation. Reaction parameters like oxidants, solvents, temperature, and reaction time were optimized for the model oxidation reaction involving diphenylmethane (DPM) as a substrate. The results obtained indicate that the substrate having benzylic sp^3 C–H bond energy less than 90 kcal/mol can be easily oxidized to the corresponding carbonyl compound in the presence of these nanocrystals at RT with stirring the reaction mixture over the bar magnet (up to 92% conversion). The oxidation of Cu_2O to CuO occurs all together with the progress of the reaction when carried out under typical aerial atmosphere in the presence of light (daylight and mercury compact fluorescent lamp (CFL) tubes prevailing in the laboratory). However, this can be avoided when the reaction was carried out in the dark or inert atmosphere or continuous flow of oxygen gas. A reaction mechanism has been proposed based on the free radical scavenger experiments and other special experiments. Also, the chemical events that occurred in the proposed reaction mechanism have been supported by mass spectral and electrochemical analysis, density functional

Cu_2O (111) facets for Benzylic C_{sp^3}-H bond Oxidation